Interactions between silver nanoparticles and fluorescent phytochromes from *Deinococcus radiodurans*

Master's Thesis, 30.8.2017

Author:

LAURI NUUTTILA

Supervisors:

JUSSI TOPPARI AND HELI LEHTIVUORI

UNIVERSITY OF JYVÄSKYLÄ

Abstract

Nuuttila, Lauri

Interactions between silver nanoparticles and fluorescent phytochromes from
Deinococcus radiodurans

Master's Thesis

Department of Physics, University of Jyväskylä, 2017, 86 pages

Applications using a cross-disciplinary approach are a common phenomenon in recent scientific research. A good example is the field of living tissue imaging where better biological labels are constantly searched with the help of physics and chemistry. In this Thesis, a near-infrared template combining silver nanoparticles and phytochromes was synthesized. The formation of the complex was confirmed by using optical spectroscopy, electrophoresis and electron microscopy. Promising fluorescent properties were obtained using monomeric chromophore binding domain (CBDmon) of a phytochrome from *Deinococcus radiodurans*. In the presence of silver nanoparticles, CBDmon showed 20% increased quantum yield and 30% decreased exited state lifetime. The brightness of the synthesized complex was 470±40% at 390 nm excitation wavelength and 134±11% at 630 nm relative to the brightness of pure CBDmon. It is likely that these promising properties could be improved by further engineering using variety of methods. Thus, the results indicate a new way to design applicable NIR-labels.

Keywords: Plasmon, brightness, imaging, CBDmon, absorption, fluorophore, quantum yield, radiative, lifetime

Tiivistelmä

Nuuttila, Lauri
Interactions between silver nanoparticles and fluorescent phytochromes from
Deinococcus radiodurans
Pro Gradu -tutkielma
Fysiikan laitos, Jyväskylän yliopisto, 2017, 86 sivua

Poikkitieteelliset sovellukset ovat viime aikoina yleistyneet tieteellisessä tutkimuksessa. Tämä näkyy hyvin esimerkiksi elävän kudoksen kuvantamisen kehittymisessä, jota varten etsitään jatkuvasti parempia biologisia leimoja fysiikan ja kemian keinoin. Tässä tutkielmassa on kehitetty ensimmäinen lähi-infrapuna-alueen fluoresenssileima, joka hyödyntää hopeananopartikkeleja ja fytokromeja. Kompleksi on syntetisoitu itse ja sen rakenne on todennettu optisen spektroskopian, elektroforeesin ja elektronimikroskopian keinoin. Lupaavat fluoresenssiominaisuudet saatiin käyttämällä monomeerisen *Deinococcus radiodurans* -fytokromin kromoforia sitovaa domeenia (CBDmon). Hopeapartikkelien läsnäollessa CBDmonin kvanttisaanto kasvoi 20 % ja viritetyn tilan elinaika laski 30 %. Syntetisoidun kompleksin kirkkaus verrattuna CBDmonin kirkkauteen oli 470±40% 390 nm:n ja 134±11% 630 nm:n virityksellä. Näitä tuloksia voidaan todennäköisesti vielä kasvattaa, koska kompleksin rakennetta on mahdollista muokata monella eri tavalla. Siksi voidaan todeta, että kehitetty menetelmä on lupaava keino lähi-infrapuna-alueen leimojen suunnitteluun.

Avainsanat: Plasmoni, kirkkaus, kuvantaminen, CBDmon, absorptio, fluorofori, kvanttisaanto, säteilevä, elinaika

Preface

The work presented in this thesis has been carried out during the years 2016-2017 at the department of Physics, Nanoscience Center and University of Jyväskylä.

Jyväskylä, September 2017

Lauri Nuuttila

Publication

The methods and results of the Thesis were based on the work contained in the following publication:

Enhancing fluorescence of monomeric bacteriophytochromes by plasmonic nanoparticles

Lauri Nuuttila, Kosti Tapio, Tibebe Lemma, Janne A. Ihalainen, Nikolai V. Tkachenko, Jussi Toppari, and Heli Lehtivuori

Submitted

Author's Contribution

The work was designed together with Dr. Jussi Toppari and Dr. Heli Lehtivuori. All the studied samples were fabricated and the measurements carried out by the Author, excluding the parts that concern protein purification and pump-probe experiments, in which the Author was also involved. The Author made the majority of the data analysis. The Author has prepared and written the first drafts of the Figures and the Publication, respectively.

List of Abbreviations

AgNP - Silver Nanoparticle

AgNP-BCML - BCML covered silver nanoparticle

AgNP-CBDmon - BCML and CBDmon covered silver nanoparticle

BCML - N_α,N_α-bis(carboxymethyl)-L-lysine hydrate

BV - Biliverdin IXα

CBD - Chromophore Binding Domain

CBDmon - Monomeric Chromophore Binding Domain

DADS - Decay associated difference spectra

DrBphP - *Deinococcus radiodurans* phytochrome

EADS - Evolution associated difference spectra

ESA - Excited state absorption

ET - Energy transfer

GFP - Green fluorescent protein

GSB - Ground state bleach

IRF - Instrument response function

LSP - Localised surface plasmon

LSPR - Localised surface plasmon resonance

MEF - Metal enhanced fluorescence

NIR - Near-infrared

NP - Nanoparticle

QY - Quantum yield

PA - Product absorption

SE - Stimulated emission

TA - Transient absorption

TCSPC - Time Correlated Single Photon Counting

TRIS - tris(hydroxymethyl)aminomethane

Contents

1 Introduction

Sensitive imaging techniques have become presently important tools on the scientific fields which deal with biology.[1–4] A commonly used method for imaging is to use labels which absorb and emit specific wavelengths of light. There are numerous alternative materials which have these properties and the repertory covers wavelengths from ultraviolet to infrared.[1,2] However, the fluorescent labels are exploited also for the intracellular purposes which sets strict terms for the properties of the label.[2,4] For example, the label must be small enough to fit properly inside the cell, it has to be stable, should not interact with cell components and the label should not be toxic for the cell. In addition to these terms, the absorption of tissue has also to be considered.[5]

New techniques and materials are constantly developed for *in vivo* imaging and the superior probes are sought among biological materials.[6] Biological labels are fluorescent proteins which are derived from living organisms and harnessed to spectral purposes with suitable modifications. A widely used label is green fluorescent protein (GFP) which has a suitable size, is stable in varying environments and does not interact with the cell components.[7] However, GFP and its variants have a disadvantage of fluorescing on the green to orange region where the tissue extinction is high compared to the near-infrared (NIR) region.[5,8,9] The extinction of the tissue diminishes the fluorescence and thus limits the usage of the GFP in imaging. Some functional NIR-labels are developed by now but they have problems with stability and/or toxicity.[1,3] Good examples are squaraine, phthalocyanine and cyanine derivatives. The problem exists also with other promising fluorophores and thus the applicable NIR-label is still under research.[10]

Recently, the search has spread among phytochromes which are studied and engineered due to the absorption and fluorescence near NIR region.[10–15] Phytochromes are red light absorbing photoreseptors which quide, e.g., photosynthesis, cellular growth and orientation in plants, fungi and bacteria.[16,17] A promising engineering template of biologically friendly fluorophore is *Deinococcus radiodurans* phytochrome and specially the chromophore binding domain (CBD) of it.[11,18] Furthermore, CBD has been rationally mutated into monomeric form to reduce the size (67 → 37 kDa) and thus increase the utility as a fluorophore.[11,18,19] CBD and

its derivatives are now researched intensively and the awareness of the fluorescence properties of phytochromes increases constantly.[10,20]

The photoactivity of CBD is based on the chromophore molecule Biliverdin IXα which binds into the protein structure.[21,18] The fluorescence quantum yield in CBD is relatively low and improvements are searched via research.[12] Succesful engineering is published using site selective mutations[10,11,19] but still relatively low fluorescence gives motivation to further engineering.

The fluorescence properties can be modified also using the environment where one can create new favourable pathways for fluorescence. This may be done with metal enhanced fluorescence (MEF) which is formerly used to increase fluorescence of dyes,[22] quantum dots[23] and green fluorescent protein.[24] The advantageous effects are based on the interactions between excited-state fluorophore and plasmonic excitation of free electrons in metal. These interactions can increase the photostability of the fluorophore by shortening fluorescence lifetime and increase the total amount of fluorescence.[25]

MEF applications in small size can be achieved using metallic nanoparticles (NP) which are small pieces of bulk metal with variable size and shape.[24,26–30] They can be grown from atoms using regular wet chemistry in the laboratory which makes them an accessible ingredient for everyone.[31] The general definition for NPs refers to prefix nano (10^{-9}) and it defines that one dimension of the particle is less than 100 nm. The small size makes NPs to fit for the tiniest applications[32,33] and allows confinement of the visible light into subwavelength sized localised surface plasmons (LSP).[34,35] Incoming electric field induces oscillating charges in the NP resulting a LSP. The oscillations induce an exponentially decaying local electric field near the NP surface and these fields may be utilized to modify the energy states of a fluorophore.[36] For example, the LSP of a silver nanoparticle (AgNP) may interact with excited electron states of a biomolecule and increase the amount of emitted photons by creating more stable and faster radiative energy channel via surface plasmons.[24] The channel is a favourable radiative pathway for the excited states of the fluorophore which decreases the portion of otherwise occurring nonradiative relaxation.

In this Thesis the fluorescence properties of fluorescent monomeric CBD

(CBDmon) were engineered with plasmonic AgNPs. CBDmons were successfully attached chemically into AgNPs and the resulting interactions were studied by optical means. A detailed analysis of spectroscopic properties revealed a new method to improve phytochromes as fluorescent labels. The method was not used until now but it offers a promising basis for label engineering.

2   Theoretical Background

The subject where a silver nanoparticles (AgNP) and a phytochrome are brought into a distance where they interact is new in the scientific field. Interactions in the systems are complex and a convenient way to approach the theory is to start with the free-space energy states of the phytochrome and AgNPs. The non-coupled states form the basis of the system which will be modified further when interactions between particles and the phytochrome are taken into account. Thus, the theory is divided into three main parts which consider about the structure and optical properties of used phytochrome named monomeric chromophore binding domain (CBDmon), formation of localised surface plasmon resonance (LSPR) in AgNPs and changes in the optical properties due to the interactions between the two systems. First, the structure of CBDmon is examined.

2.1   Structure and Spectral Properties of Chromophore Binding Domain

Chromophore binding domain (CBD) is a part of a dimeric bacteriophytochrome from *Deinococcus radiodurans* (DrBphP) which consists of amino and carboxyl terminal modules (Fig. 1).[17,18] The amino module forms of PAS (Per/Arndt/Sim), GAF (cGMP phosphodiesterase / adenyl cyclase / FhlA) and Phytochrome associated (PHY) domains from which PAS and GAF domains together have a general nomination as CBD.[21] The nomination arises from the fact a chromophore molecule binds into the phytochrome in the binding pocket located in CBD. The carboxyl terminal module is an output module of the phytochrome and it consists of histidine kinase domain (HK).[17,18] At present, DrBphP are expressed in bacteria and recently also the dimeric and monomeric forms of CBD have been produced lead-

ing to the accurate analysis of their structure.[21,11] As shown in Fig. 1, CBDmon can be derived from a dimeric full length phytochrome by removing PHY, HK and one of CBD domains.[11,19] The resulting structure is smaller than full length phytochrome or dimeric CBD and it sustains the photochemical abilities.[12] These regions, where photochemistry takes place, have been subjects of high interest and thus the presence of Biliverdin IXα (BV) chromophore has been discovered.[21]

BV is a chromophore molecule which allows the photochemical reactions in DrBphP.[21] In Fig. 1 can be seen the structure of BV in non-illuminated red absorbing (P_r) conformation.[21,38] The structure alters when a phytochrome is illuminated but it is discussed more when a photocycle of CBD is reviewed. BV is covalently bound into cystein 24 in the protein backbone which anchors the chromophore into the phytochrome.[21,18] The conformation of protonated BV is stabilised by hydrogen bonding and salt bridges to nearby amino acids.[21,18,39] The stabilising effect is due the large bonding network where the polar propionate groups ($R-COO^-$) and pyrrole rings($R-C_4H_2NCH_3-R$) of BV are organized to fit the surroundings. The main part of the network are His-260, His-290 and Asp-207 which can be found in all Phytochrome superfamily.[39,40]

To obtain information about the properties of phytochromes the spectroscopic measurements of absorption and fluorescence are usually done.[20] Understanding of the results demands the further knowledge about the spectroscopic properties of BV and the photoconversion. The origins of QY have also to be mastered. The theory of these properties is presented next.

2.1.1 Biliverdin as an Origin of the Absorption and Fluorescence

Closer examination of BV structure in Fig. 1 reveals that it is a conjugated system with numerous alternating single and double bonds. Thus, it is capable of absorbing light which occurs in visible wavelengths.[38] The absorption characteristics of free BV is presented with red color in Fig. 2 where two absorption bands (Soret and Q band) appear. Soret band is located near 400 nm while the wavelength and shape of Q band varies (500-750 nm) in different measurement conditions.[38] The origin of the two peaks can be explained using analogy to porphyrin which is a similarly conjugated system and from which BV is reduced.[41,42] Both Soret
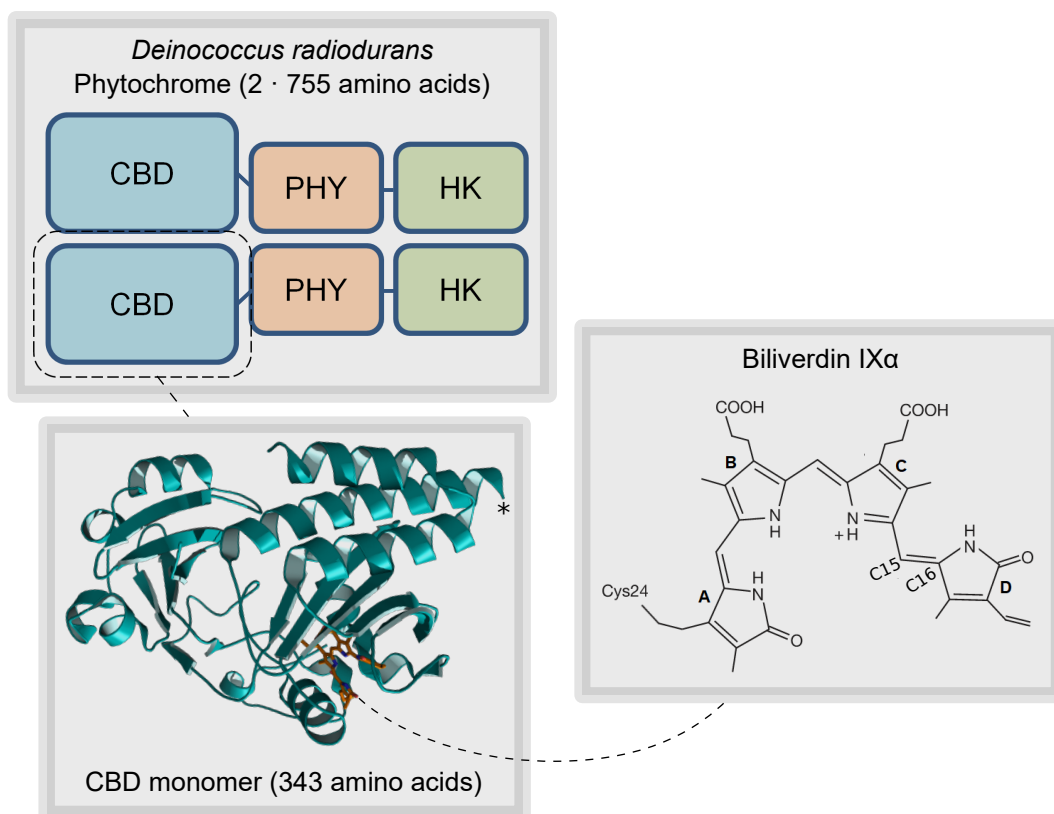
Figure 1: A schematical structure of phytochrome from *Deinococcus radiodurans* which consists of chromophore binding domain (CBD), phytochrome assosiated domain (PHY) and histidine kinase (HK) as a dimeric structure.[11,21,37] Primary photochemical reactions occur in CBD domains of which a three dimensional structure is presented in the lower left corner.[11] * indicates the location of the polyhistidine tag. On the right is the molecular structure of Biliverdin IXα which is bound into cystein 24 in the protein backbone and gives CBDmon the photoactive properties by isomerization.[21,38] The carbons 15 and 16 in the isomerization site are labelled into the structure.
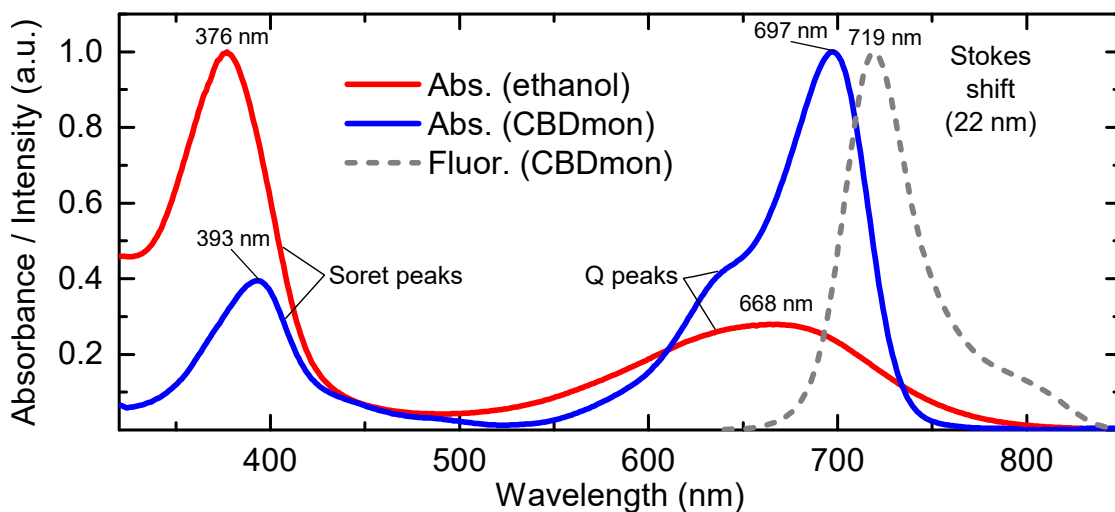
Figure 2: Normalized absorptions of Biliverdin IXα free in ethanol[43] (red) or attached to CBDmon in pH 8.0[44] (blue). Fluorescence of CBDmon is drawn by grey dashed line.[11] Absorption maximums of each band are labeled next to the peaks.

and Q band arise from electronic π-π^* transitions and they are affected by the modification of the chromophore structure. From these two, especially Q band is discovered to be sensitive for changes of the vicinity of π-orbitals.[42]

The changes in the absorption properties are seen in the previously measured data which is obtained using different chemical and biological environments with BV and other similar tetrapyrroles.[10,11,38,39,45,46] Overall, one can say the variations in pH, temperature and chemical properties of the solution reshape the absorption.[38,42,45] In addition, the reshaping can be triggered also by mutating adjacent amino acids of the chromophore.[11,10,39] The mutations alter the orientation of the chromophore and thus the interactions to binding pocket.[10,47] In CBDmon, the fixed orientation produces an absorption presented with blue color in Fig. 2. The impact of the accurate orientation can be seen in the spectrum where the shape of Q band is narrow and intense compared with the free BV spectrum. The restricted movement of BV restricts also the amount of possible excitations which raise the probability of only a few transitions.

The optical activity of BV can be followed also by studying the radiative pathway to relaxation after photon absorption.[11,12] Absorbed photon strains C15=C16

double bond which is relaxed by the interactions with the vicinity of the chromophore.[11] The relaxation occurs via competitive non-radiative and radiative pathways.[39] The non-radiative relaxation can take place via isomeric conversion of the double bond, which leads to the conversion in whole phytochrome.[21, 48] Another proposed non-radiative pathway are various internal conversions which dissipate the excitation energy, e.g., via charge transfers into the protein vicinity.[49]

A part of the excitations is followed by fluorescence which occur usually from the lowest excited electron state of a given multiplicity.[12, 36] This is called Kasha's rule and it states that the relaxation to the lowest exited state occurs much faster time scale than fluorescence would happen.[50] Combined with a Franck-Condon principle, the shape of the fluorescence is in most cases a mirror image of the absorption band which represents the lowest exited state.[36] In the case of CBDmon, the fluorescence is rare and only approximately 2.9% of absorbed photons are emitted from the excited ground state.[12] Closer examination of the spectrum (Fig. 2) shows a Stokes shift of fluorescence from 697 nm to 719 nm.[11] However, one can see also the unique shape of the fluorescence which does not correspond to the behaviour described above. The difference can be explained with the heterogenity of the sample which can be seen in many biological photoreceptors.[49] Thus, it is possible that the absorption is a superposition of two states of which only one is fluorescent.

2.1.2 Optical Measures for Fluorescence

To generate efficient fluorescence, the radiative rate of a chromophore must be competitive with the rates of non-radiative processes.[36] With previously defined absorptive and emission properties, the full-scale comparison of fluorophores is still a struggle. A single absorption spectrum gives information about the energy structure (wavelength of the absorbed photon) and the concentration about the absorbent (Beer-Lambert law) but the emission can not be connected into the properties of the sample.[51] The problem can be corrected by linking the absorption properties into the emission when the information about the sample concentration is included.[36, 51] Knowing the intensity of the emission with a known concentration

gives two commonly used spectral methods to measure the emission properties of the fluorophore.[36,52] These methods are presented next.

First of the methods is called quantum yield (QY) which ($\Phi_\mathrm{f} = \gamma_{Em}/\gamma_{Abs}$) compares the amount of emitted photons γ_{Em} from the sample to the amount of absorbed photons γ_{Abs} into the sample.[36] It can be measured with relative or absolute methods from which the relative method is commonly used when the optical properties of the sample and reference do not vary significantly.[53] QY is then obtained comparing the sample fluorescence to a reference with given QY using a proportion

$$\Phi_\mathrm{f} = \Phi_\mathrm{f,R} \frac{F}{F_\mathrm{R}} \frac{OD_\mathrm{R}}{OD} \frac{n^2}{n_R^2}, \tag{1}$$

where subscript R refers to reference sample, F is integrated fluorescence, OD is optical density and n is refraction index of the medium in the sample.[36] In the situations, when the samples do not affect significantly to n and they are measured both in identical mediums, the refractive indexes can be cancelled. Furthermore, the optical density can be expressed as $OD = A \ln 10$, where A is absorbance of the sample.[36] Hence, in the identical measurement conditions the Eq. (1) simplifies to

$$\Phi_\mathrm{f} = \Phi_\mathrm{R} \frac{F}{F_\mathrm{R}} \frac{A_\mathrm{R}}{A}, \tag{2}$$

which is a general expression for measuring the QY of the sample with spectroscopic methods.[11,10,12,36]

Another of the methods, called brightness B, considers also the absorption properties of the fluorophore. The definion of brightness is

$$B = \Phi_\mathrm{f} \varepsilon(\lambda_\mathrm{ex}), \tag{3}$$

where Φ_f refers to QY, and $\varepsilon(\lambda_\mathrm{ex})$ to the extinction coefficient at the excitation wavelength.[53] QY enables the comparison of the photon emission efficiencies but focusing the analysis only to the emission can make one forget a fact the process is a combination of absorption and emission. Fluorophores are developed ultimately for imaging purposes and also the absolute intensity during the imaging is crucial.[2]

It is now reviewed that the radiative processes of CBDmon can be studied using
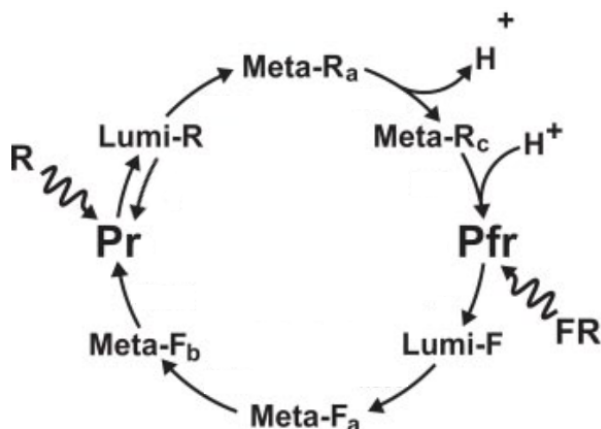
Figure 3: A proposed stepwise mechanism of the CBDmon isomerization after red (R) or far-red (FR) light illumination.[20,39] Excitation starts the structuric conversion from P_r or P_{fr} states to the other main conformation via Lumi- and Meta-states. The conversion occurs via different pathways and hence it can be represented as a cycle. Edited from Wagner et al.[39]

optical spectroscopy. However, when the dimension of time is taken account, it can be used also to obtain information from the non-radiative behaviour.[20] However, to understand time-resolved measurements one has to know what happens inside CBDmon. Thus, the theory of photoconversion is first introduced.

2.1.3 Photoconversion and Time-Resolved Spectroscopy

The relaxation of the excited state in CBDmon was earlier mentioned to occur partly via conversion of the whole phytochrome. The process has a general name photoconversion and, in CBDmon, it occurs stepwise in a cyclic model including BV isomerisation and proton transfer reactions.[11,20,39,54] (Fig. 3) CBDmon has two main conformations (P_r and P_{fr}) which are named by red and far-red light they absorb.[21,54] The conversion occurs in both directions between these states and it is driven onward by even a small illumination.[16,21,54] Thus, in optical measurements, illumation leads to the situation where P_r and P_{fr} are mixed. Therefore the data is measured mainly from non-illuminated P_r state phytochromes.

Photoconversion is a competitive process for fluorescence and understanding

the conversion gives more detailed information about the behaviour of the phytochrome.[20] It is known that the bonding of the BV into Cys-24 exists during the photoconversion.[39,55] The covalent bond maintains the interactions with the binding pocket and the conversion have been seen to affect spectroscopic data with other similar phytochromes.[49,56,57] The network around the chromophore begins to alter when an incoming photon is absorbed and the photoconversion starts.[55] BV is exited into P*-state which means strained C15=C16 double bond due the additional energy absorbed.[11] As presented earlier, excitation relaxes usually with internal conversions but a part of the population remains exited and the isomerisation of the double bond occurs. The bond rotation reaches the first energy minimum (Lumi-R state) after which a proton is released from BV and bound into pyrrole water or one of the residues.[11] At this stage the residues around the D-ring of the BV are important in the conversion process because the structures of the residues are altered due the new energy minimum.[39,40] It is shown that Asp-207, His-260, His-290, Tyr-176, Tyr-263 and Phe-203 have important role in the process and mutating these amino acids blocks further conversion.[39] The orientation of the vicinity of the binding pocket triggers also secondaric changes in the phytochrome structure.[55] After the reformation the lost proton is recovered to BV and the system results to P_{fr} stage where all the nitrogens are protonated.[39] The conversion back to P_r state occur via different route but closer analysation is not necessary in this context. Further information can be found in Ref.[54]

The photoconversion of phytochromes is a fast process occuring during a time scale from picoseconds to milliseconds. For example, the Lumi-R formation is detected to occur in tens of picoseconds while formation of the P_{fr} state takes milliseconds to form.[39,57] The different orders of the magnitude lead to the situations where the shortest events are impossible to measure due the low resolution with long measuring time. Respectively, the amount of the data becomes too large if the resolution is increased to fit for measuring short time scale events. Therefore the methods for measurements are selected carefully to fit for the needs.
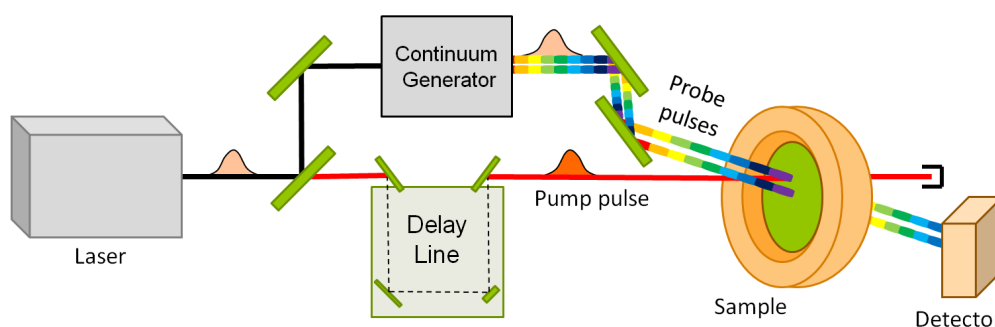
Figure 4: A schematic figure of the ideal mechanics used in transient absorption measurements. The sample is exited with a short laser pulse (pump pulse) which travels through the sample after which it is trapped. The probe pulse (black) is separated from the original laser pulse and directed to continuum generator. The generated continuum of wavelengths (rainbow colors) is divided into separate beams and directed to the sample. One of the pulses travels through the exited sample area and one through non-illuminated area. The beams end to a photo detector where the absorbance is recorded as a function of wavelength. Edited from Tkachenko.[59]

2.1.4 Analyzing the Photocycle with Transient Absorption Spectroscopy

Transient absorption (TA) spectroscopy is a powerful tool for short time scale measurements due to the present highly tuned optical systems which can observe processes occuring in femtoseconds.[58,59] As presented in Fig. 4, the sample is excited with a pumping laser pulse after which the absorption of the sample is recorded with a probing laser pulses during defined period of time. Both pulses are generated with a single laser source which generates short femtosecond pulses.[59] First, the laser beam is amplified and split into pump (red) and probe (black) beams. The pump beam is directed into the sample for excitation. The probe beam is directed into white light continuum generator where it is focused into a sapphire plate (rainbow colors). The generated beam is splitted into two and both beams are directed through the sample into a photo detector (a charge-coupled device or a photodiode array). The two beams are recorded as signal and reference beams from which the signal beam is focused into the area where the pump beam has excited the sample and the reference beam to the area with the ground state sample.

The absorption difference $\Delta A(\lambda)$ of the two probe beams is calculated as a function of wavelength λ.[58,59] To obtain a dimension of time into the data set, the length of the optical path of pump (or probe beam) is modified with a delay line. This can be done by moving a corner reflector to increase/decrease the path length. As a result, the $\Delta A(\Delta t, \lambda)$ spectrum is obtained where the absorption difference is measured after a delay time Δt from the sample excitation. The absorption of a single wavelength can also be plotted as a function time which is called kinetic trace.[58] The data is usually analysed further with global analysis techniques which are named as evolution- or decay associated difference spectra (EADS/DADS).[58,60] In both models, all the kinetic traces are fitted as an entirety with a number of independent exponential decays (with τ) and their amplitudes which mimic the measured data and thus the energy states of the system. In DADS the decay processes do not affiliate with each other and the decay of energy states is independent.[60] In EADS the decay processes occur sequentially and it represents the spectral evolution of the data.[58,60] Both analysis techniques lead to difference spectra with reduced background noise.

After analysis of the data, the interpretation has still to be done. It is not always straightforward due to the various processes which may overlap with each other spectrally.[58,60] In general, the processes of ground state bleach (GSB), stimulated emission (SE), excited state absorption (ESA) and product absorption (PA) are usually observed.[58] GSB is related to the loss of the ground state molecules which are exited by the pump pulse. The absorption of the ground state decreases due to the loss of the molecules which gives a negative signal to difference spectrum. SE occurs when the excited sample is hit by a probe pulse. The incoming photon induces a relaxation of excited electron which produces a photon to a direction where the probe photon was proceeding. Thus, the induced emission travels also to the photo detector and it is observed as negative absorption. The shape and energy of SE follow the spectral profile of fluorescence. Because SE is caused by the probe photons it is proportional to the intensity of probe beam. The positive signal to the spectra may be caused by ESA and PA, from which ESA is observed when the exited molecules absorb the wavelengths of the probe beam. The positive signal is focused on the region of absorption. PA is produced by the photochemical

material which generates long-living molecular states via e.g. isomerization. In this situation also GSB appears because the altered population has left the ground state.

The TA measurements are a fascinating method to study systems including CBDmon because they may provide valuable information about the changes in the relaxation mechanisms in the system. These properties, in the presence of AgNPs, are further reviewed in Section 2.3. However, for CBDmon, former TA measurements have not been published but results from similar phytochromes can be found.[57,49] Thus, it is likely the TA spectrum of CBDmon shows the features that were previously reported. For example, the formation of Lumi-R state can be seen in the results with a non-decaying product and red-shifted absorption (PA). From literature, it is known that the Lumi-R state is a requirement for the photoconversion from P_r towards P_{fr} state.[11,49,54,61] Thus, it is likely the confinement of the conversion removes the photoproduct from the difference spectra.

2.1.5 Analyzing the Photocycle with Time-Correlated Single Photon Counting

In a system which includes many optical processes, the interpretation of the TA data is often tricky and requires other methods for support. With a fluorescent sample, a possibility is to examine the emission properties of the excited states and determine their lifetimes τ.[36] The determined τ can be compared with the results from TA measurements to identify the kinetics of the excited state. τ can be determined by measuring the emission of the sample directly as a function of time using time-correlated single photon counting (TCSPC) setup.[59,62] (Fig. 5) With a resolution of picosecond scale, the lifetimes down to tens of picoseconds can be determined accurately.

In TCPSC, the sample is excited with a short laser pulse after which the delay of the emission is detected as function of time.[59,62] First, a short laser pulse is generated at computationally defined time point which is directed into the sample. The laser pulse excites a fluorophore in the sample which is then relaxed and randomly emits a photon within the sample specific τ.[36] Photons emitted into the direction of a photo detector are detected and the elapsed time is added into a

histogram.[59,62] After the arrival of the photon the measurement is stopped and the excitation-emission cycle is restarted. If the photon is not detected the cycle is restarted after a defined period of time. The measurements are repeated until desired amount of data is acquired. All the acquired data is combined into a single histogram which represents the decay of a number of fluorophores in the excited state A. The fluorescence decay is known to be exponential and many fluorophores have also multiple simultaneous decay processes. Thus the lifetime can be obtained from equation

$$N(t) = \sum_{i=1}^{n} A_i e^{-t/\tau_i}, \tag{4}$$

where $N(t)$ is the excited state population and t is the elapsed time from excitation.[36] The exponential decay(s) are then fitted to data to resolve the lifetime(s).[59,62] During the fitting one has to take note of the instrument response function (IRF) which represents the timing inaccuracy occurring in all measurement configurations due to a time-lapse in detector, laser and other electronics. The variation of the timing leads to the spreading of optical response (from the ideal narrow peak to resemble a Gaussian shape) and the same peak is included also in the measured photon distribution due to scattering from the sample. To consider the effects of IRF, it is usually measured using a scattering sample and the obtained photon distribution is then included into iteration of decay fits (reconvolution).[63] As a result, one obtains the real decay curve(s) and lifetime(s).

Acquiring the fluorescence lifetime gives also another perspective to the analysis of the optical propertis of CBDmon. For example, it is showed that the presence of plasmonic metal may affect to the fluorescence lifetime and QY in a specific way.[36] Thus, measuring τ of the samples gives valuable information about the reasons behind the possible optical changes. These effects are discussed in the Section 2.3. First, to understand the plasmonic effects, the theory is focused into the field of metallic nanoparticles (NP).
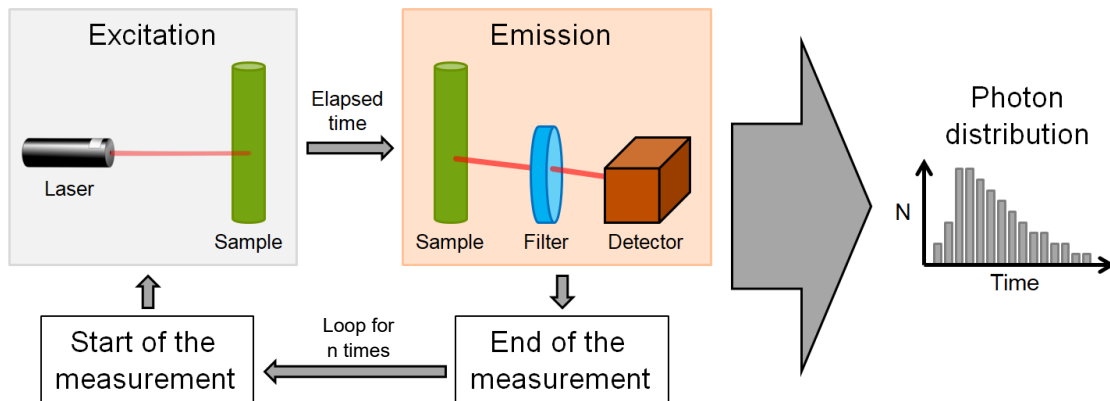
Figure 5: A schematic figure of the mechanics used in time-correlated single photon counting experiments. The sample is excited with an appropriate pulsed laser after which the elapsed time to the photon emission is measured with a photo detector.[59,62] The accuracy of the measurements is usually increased using a filter in front of the detector which allows transmission of photons only in the region of fluorescence. The measurement is repeated until an appropriate photon distribution is obtained after which the lifetime of the excited state is resolved computationally.

2.2 Surface Plasmon Polariton in Spherical Metal Nanoparticles

Metallic NPs are small pieces of bulk metal which absorb and scatter different wavelengths of light. They have a high surface area to volume ratio and appear with varying size and shape. Recently, it is shown that NPs made from noble metals (especially silver and gold) have ability to confine the light into localised surface plasmons (LSP).[34,35] LSP is quanta of collective and resonant mechanical oscillations of the free electrons in metal combined with oscillating electric fields outside the metal. These states can be excited by photons or directly by the energy of the molecular excited state via non-radiative energy transfer (ET). Same can happen also other way around, i.e. LSP can excite molecule directly like a photon in a more convenient case.

The properties of metallic NPs are often described by the means of optics. However, the treatment of absorption and scattering of light by small particles

is a problem in electromagnetic theory. This theory is influenced by electricity, magnetism and polarization of light. Thus, some simplifications is often done to understand the phenomenon without numerical calculations. One of the frequently used methods is the Drude-model.

2.2.1 Localised Surface Plasmon Polariton Resonance Conditions

The LSP excitations in NP have always a certain resonance condition, i.e., a wavelength with which the LSP has the highest intensity and coupling cross-section. This called a localized surface plasmon resonance (LSPR).[34] The NP properties which determine the LSPR wavelength are the material, size and shape of the NP and the refractive index of the environment. Effect of the material and environment to the can be examined with Drude-model where NP has conductive electrons between ionic crystal structure as free electron gas or electron plasma.[34,64] The free electrons begin to oscillate when the metal is exposed to external electromagnetic field. On the other hand, the charge polarization in NPs can be modeled with polarizability α which describes the charge separation in NPs induced by external field. (See appendix 1) Handling the oscillations within the boundaries of α gives information about the oscillation frequency.

Properties of the metals are usually described with dielectric function $\varepsilon(\omega) = \varepsilon^{'}(\omega) + i\varepsilon^{''}(\omega)$ which is also called sometimes as relative permittivity.[34,64] ε is a complex quantity in which ε' can be linked to the polarization response and ε'' the optical quality of metal which are both unique for different elements.[65,66,67] The resonance frequency of LSPR can be determined from ε' which is thus a key part in the selection of used material.[34,66] ε'' modifies the bandwidth and height of the LSPR and thus affects the quality of the optical applications and the existence of LSPR.[65,66,67,68]

In Drude model the real (ε') and imaginary (ε'') parts of the ε are defined as

$$\varepsilon^{'}(\omega) = 1 - \frac{\omega_p^2}{\omega^2 + \gamma^2} \tag{5}$$

and

$$\varepsilon^{''}(\omega) = 1 - \frac{\omega_p^2 \gamma}{\omega(\omega^2 + \gamma^2)}, \tag{6}$$

where $\omega_p^2 = \frac{ne^2}{\varepsilon_0 m}$ is a plasma frequency of the free electron gas in metal and γ a collision frequency which acts as a damping factor of the electron oscillation.[34,64] The plasma frequency ω_p^2 depends on the density of free electrons n, the effective mass of an electron m and dielectric permittivity of free space ε_0.[34] In all metals ω_p is situated within invisible UV-range, but in silver and gold it locates closer to visible range than in other metals.[68] From the viewpoint of optics this is an advantage, as the inner losses in metal decrease near the resonance wavelength and the plasmonic character becomes dominant.[34] From these two, silver has the range of LSPR reaching further to the higher frequencies and thus it suits better to interact with the Soret band of CBDmon.[68,69]

For larger frequencies near ω_p, the dielectric function consist mainly of ε' because ε'' of becomes small.[34] As stated, in silver this applies in visible region and ε' can be considered relatively large compared with ε''. Thus, the analysis can be focused on the real part of the ε.[64] Silver has also relatively low collision frequency and with reasonable approximation of $\omega \gg \gamma$ the ε can be considered as

$$Re[\varepsilon(\omega)] = 1 - \frac{\omega_p^2}{\omega^2}. \tag{7}$$

Now the boundaries of

$$\alpha = 4\pi a^3 \frac{\varepsilon - \varepsilon_m}{\varepsilon + 2\varepsilon_m} \tag{8}$$

are applied for which the detailed derivation can be seen in Appendix 1. LSPR occurs at Fröhlich condition which means that the charge separation in NP is at maximum. This will cause also α to be at maximum.[64] The highest α of the AgNP is achieved when $|\varepsilon + 2\varepsilon_m| \to 0$ and therefore $\varepsilon(\omega) \to -2\varepsilon_m$. Thus, the dielectric function is in form of

$$Re[\varepsilon(\omega)] = 1 - \frac{\omega_p^2}{\omega_L^2} = -2\varepsilon_m, \tag{9}$$

where ω_L is the LSPR frequency. To make the presentation more familiar, the equation (9) can be modified to the function of wavelength λ by substituting $\omega = 2\pi c/\lambda$. The substitution gives the form of

$$\frac{\omega_p}{\omega_L} = \frac{\lambda_L}{\lambda_p} = \sqrt{1 + 2\varepsilon_m} \tag{10}$$

and furthermore

$$\lambda_{\mathrm{L}} = \lambda_p \sqrt{1 + 2\varepsilon_m}. \tag{11}$$

This is the LSPR condition where the interactions between AgNP and light are highest. LSPR wavelength λ_{L} is affected by the characteristic plasma wavelength λ_p of the silver and a factor modified by the dielectric function of the medium ε_m. From here can be seen that the surrounding of the particle affects the optical properties by shifting the LSPR wavelength. However, the approximations have dropped the information about the geometry which affects also to the optical activity.

The effects of the geometry can be seen from the extinction factors for scattering C_{sca} and absorption C_{abs} which can be derived from a mode derived by more advanced Mie theory. These are

$$C_{ext} = C_{sca} + C_{abs} = \frac{k^4}{6\pi} |\alpha|^2 + k \cdot Im[\alpha], \tag{12}$$

where k is a wavenumber of the radiation.[70] Both C_{sca} and C_{abs} can be seen to depend on the polarizability α and thus the particle radius a (see Appendix 1). More accurately, factors scale as $C_{sca} \propto a^6$ and $C_{abs} \propto a^3$ which shows that both scattering and absorption are strongly size dependent properties. With small NPs the efficiency of absorption is dominant over scattering due the scaling factors of a.[34] In this region photons are efficiently absorbed into LSPR. Higher exponential dependence to a indicate that scattering is a dominating property when the particle radius becomes large.

2.2.2 Determination of the Localised Surface Plasmon Resonance Wavelength as a Function of Particle Radius

The nature of LSPR in AgNP has been introduced by methods which give an insight to the physics of the energy states in the system. However, accurate theoretical values for the LSPR are complex to determine because the used theory does not include, e.g., damping and interband effects or that increasing the size of the particle decreases the restoring force of the depolarization field which red-shifts the resonance.[34] To involve everything into calculations would require high expertise

and usually numerical methods. Instead, the properties are already well determined experimentally. Therefore, it is more convenient to use the experimental values which are listed as a function of the wavelength in Ref.[69]

2.3 Interactions Between a Silver Nanoparticle and Monomeric Chromophore Binding Domain

With their complex and partly indeterminate properties, the free AgNPs and CBDmon are interesting subjects of research already by themselves. However, bringing the fluorophore to the vicinity of AgNP raises a question about the resulting interactions between AgNPs and CBDmon and the effects to the observable phenomenons like absorption and fluorescence. Potential effects may be seen, e.g., in changes in the emission rate and wavelength respect to the environmental changes.[36,71,72]

The interactions between AgNPs and CBDmon may be examined when the proteins are adsorbed into the surface of AgNP. A binding of CBDmon occurs, e.g., during a specified chemical synthesis where the edge of CBDmon is separated approximately a nanometre from the AgNPs by N_α,N_α-bis(carboxymethyl)-L-lysine hydrate-molecule (BCML).[11,31,73,74] The synthesis creates a structure illustrated in Fig. 6 and the methods are reviewed in the Appendix 2. The illustrated structure assures the favourable distances to interactions which are presented next.

2.3.1 Plasmonic Interactions Modify the Properties and are Modified by the Properties of Environment

The interactions between two separate energy systems are defined as coupling which means that energy may be transferred between the systems.[75] The magnitude of the interactions determines whether the coupling is strong (original energy states become mixed) or weak (original energy states remain).[75,76] Strong coupling, and thus mixing of the states, changes the energy structure of the fluorophore which can be seen as a (Rabi) split in a spectral data.[76] Due to the changes of the full energy structure, the chemistry of the emitter may be radically modified which opens ways for new possible applications.[77–79] However, achieving
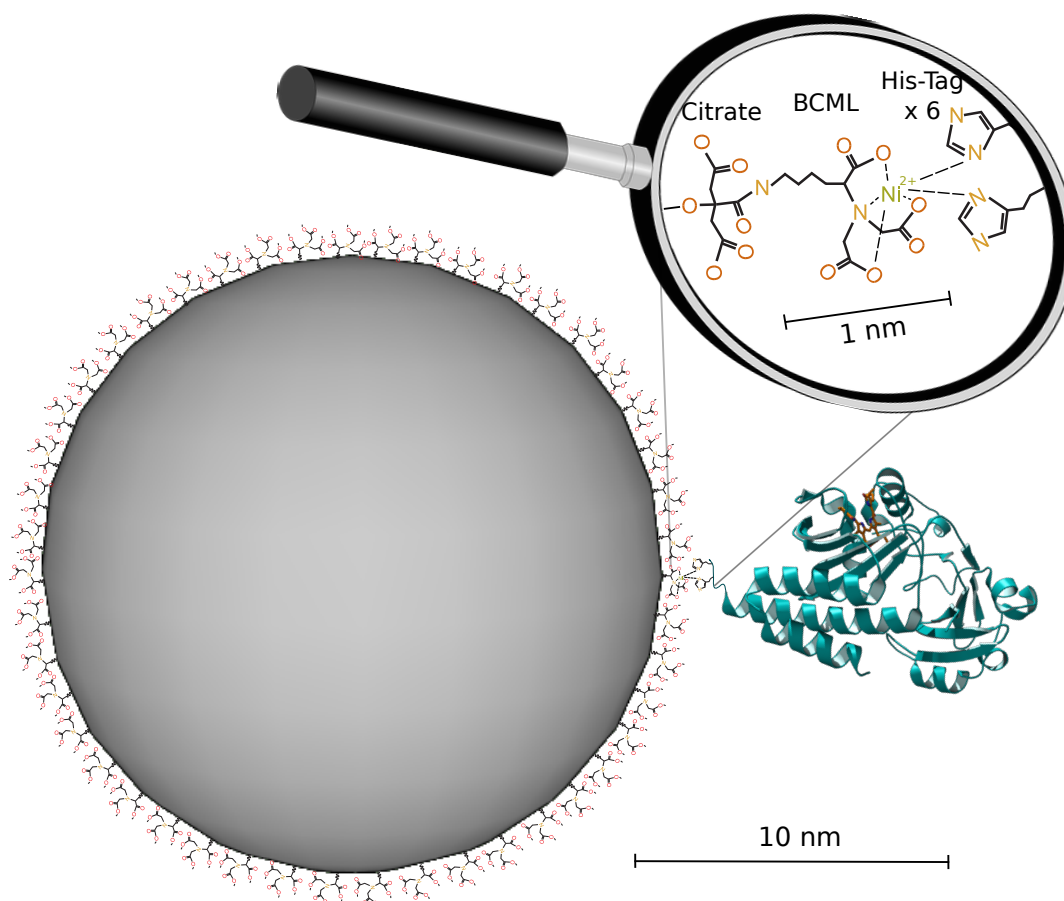
Figure 6: A schematic structure of AgNP-CBDmon complex with the magnification of the binding site. AgNPs are capped with stabilizing citrate molecules[31] to which N_α,N_α-bis(carboxymethyl)-L-lysine hydrates (BCML) are covalently bound.[73] CBDmons[11] attach to the NP surface with the help of coordination bonds formed between polyhistidine tag (His-Tag), nickel atom and BCML.[73]

a strong coupling requires special circumstances and it is rarely observed. General phenomenon is weak coupling where the wavelength of the emission is unaltered and only the emission intensity, Rayleigh scattering intensity and relaxation rates are modified.[36,76] In some cases also a distance of energy transfer (ET) may be increased.[71] When a nearby surface of metal couples with a fluorophore and boosts the properties of the fluorescence the favourable effects are called metal-enhanced fluorescence (MEF).[36,33,71]

When LSPR of a NP is focused into absorption and/or fluorescence energies of the fluorophore the plasmonic environment has an ability to improve QY and brightness of the fluorophore.[71,80–82] And vice versa, attachment of even a mono-layer of the fluorophore to NP can significantly shift its LSPR frequency, and thus to be utilized as a highly selective sensor.[83–85] Both processes are affected by a number of physical and chemical parameters concerning NPs, fluorophore and the environment which have to be carefully tuned according to the theory to significant effects.[69,71,68] However, the complicated theory can be generalized and the origins of LSPR shift and fluorescence enhancement can be represented from simpler perspective.

2.3.2 Varying Medium Shifts the Localised Surface Plasmon Resonance Wavelength

The LSPR wavelength of AgNPs was derived earlier from Drude model to be as in Eq. (11). The equation shows that the maximum of the LSPR peak is affected by the material of the NPs and the dielectric constant ε_m of the surroundings. This relation can be utilized to examine the interactions and binding ability between AgNPs and CBDmon. Experimentally, small changes in the environment have been reported to shift the absorption maximum of NPs[68,86–89] and CBDmon as a protein with large mass has a potential for large LSPR shift.[68]

However, examination of the environmental changes to LSPR conditions are inconvenient with ε_m and a conversion to more practical refractive index is generally made. ε_m can be represented as $\varepsilon_m = n_m^2$ where n_m is a complex refractive

index of the medium. Thus the Equation (11) can be represented as

$$\lambda_{\mathrm{L}} \cong \sqrt{2}\lambda_p n_m \tag{13}$$

from where the dependence $\lambda_{\mathrm{L}} \sim n_m$ can be seen. Now it is convenient to define a spectral shift $\Delta\lambda$, as an estimation for the LSPR shift in the presence of adsorbed layer on the NP surface. The shift is defined

$$\Delta\lambda = m\Delta n \left(1 - e^{-2d/l_d}\right), \tag{14}$$

where m is the sensitivity factor of the AgNP, Δn is adsorbate induced change in the refractive index ($n_{\mathrm{adsorbate}} - n_{\mathrm{medium}}$), d is the effective layer thickness of the adsorbate and l_d is the length of the decaying electromagnetic field.[68, 89]

Closer examination of Eq. (14) reveals the key properties of the NP and the adsorbate which affect to the LSPR shift. The properties of the NP are determined by material, size and shape and they all affect to the sensitivity factor. m is increased both when the width/length ratio is high and near sharp edges of the NP.[86] Also using single NPs increase m because they have narrower spectral line widths than polydisperse solution and more confined eletric field (lower I_d).[68] Increased sensitivity factor leads to larger spectral shifts which are more easily seen in the absorption spectra.

Another viewpoint to the spectral shift is to examine the change in refractive index Δn. It is showed that larger molecules like proteins often have large shifts due the large d which makes $\Delta\lambda$ clearly observable.[86–88] In addition, chromophores coupling to LSPR produce large LSPR red or blue shifts if the original maximum does not overlap with the molecular resonance of the chromophore.[90] These observations conclude that CBDmons adsorbed into AgNP surface have a potential to large $\Delta\lambda$ of LSPR which may be recognized from the absorption spectra of AgNP-CBDmon complex. However, the absolute size of the shifts is hardly predictable.[68,86–89]

2.3.3 Quantum yield and Lifetime Near Metal Surface

Properties of a fluorophore are often measured with the quantities which are closely related to the emission rate and amount of photons emitted from an excited state.[36] Modifications of these properties can be seen near a plasmonic material which modifies the energy system of nearby fluorophores.[36,72] An example is illustrated in Fig. 7 where a fluorophore with a distinct absorption and fluorescence is considered. During the excitation, coupling of LSPR and fluorophore changes the absorption cross-section of the fluorophore and the new complex includes the absorption rates of original fluorophore (k_A) and ET transferred fotons from NP ($k_{A,m}$). In the coupled system the NP may thus highly increase the total absorption rate because the field of LSPR captures fotons efficiently.[34] Increased absorption leads to increased brightness (Eq. 3) which is essential for fluorescence detection.

During the relaxation, plasmonic material attracts photons from fluorophores to surface plasmons by a higher density of states.[72,91,92] Thus, the photons are partially directed from the fluorophore to the radiative (Γ_m) and non-radiative pathways (k_m) in LSPR. From these, k_m are usually tried to be suppressed as the plasmonic losses restrict the increase of Γ_m. However, by scattering photons with a high radiative rate, properly tuned LSPR may increase the total radiative rate by high Γ_m.[82,91]

In addition to the change of the relaxation rates, the presence of the metallic NP modifies also the determination of QY. QY with no presence of metal can be defined as

$$\Phi = \frac{\Gamma}{\Gamma + k_{nr}},$$ (15)

where Γ is radiative relaxation rate and k_{nr} is non-radiative relaxation rate.[36,51] The lifetime τ is the inverse of the sum of radiative and non-radiative relaxations rates[36]

$$\tau = \frac{1}{\Gamma + k_{nr}}.$$ (16)

When the fluorophore is coupled with LSPR of the NP the equation Eq. (15) is modified into the form of

$$\Phi_m = \frac{\Gamma + \Gamma_m}{\Gamma + \Gamma_m + k_{nr} + k_m},$$ (17)
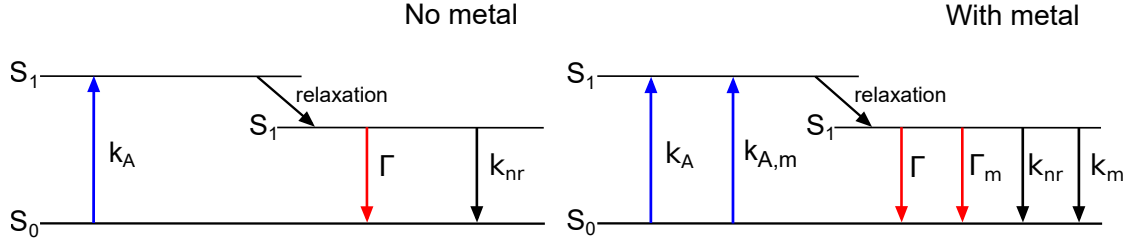
Figure 7: A Jablonski diagram of a fluorophore in free space (left) and in presence of plasmonic metal (right).[36] In free space the fluorophore absorbs fotons with absorption rate k_A which excites the molecule from ground state S_0 to excited state S_1. After solvent relaxation the excited state decays via radiative (Γ) or non-radiative pathways (k_{nr}). In the prescence of metal, photons are absorbed also to SPR from which the energy is partially transferred by ET to the fluorophore with a rate of $k_{A,m}$. The energy from the excited state may again transfer back to the SPR and the decay can occur via radiative pathways (red) or non-radiative pathways (black) of both fluorophore and metal (Γ_m,k_m).

where Γ_m and k_m are the radiative and non-radiative rates via LSPR.[36] Equation (17) shows that significant improvements to QY are acquired only when $k_m \ll \Gamma_m$ and $\Gamma_m \gg \Gamma$. That is, the changes in QY are noticed only if the metal has highly radiative nature compared to the plasmonic losses of the metal and the radiative rate of the fluorophore. The lifetime of the fluorescence is also modified and it is in form of

$$\tau_m = \frac{1}{\Gamma + \Gamma_m + k_{nr} + k_m}. \tag{18}$$

Modification of the fluorophore relaxation rates with metallic NPs have been found to enhance both radiative and non-radiative pathways.[72,91,93,94] A requirement for having positive effects of MEF is to control the rates and confine the non-radiative pathways as much as possible. This is done by engineering the parts of the complex.[82,95,96] In some experimental cases the non-radiative pathways have become dominant and the fluorescence properties are quenched.[97–99] This is avoided when the properties of the fluorophores are engineered.[36]
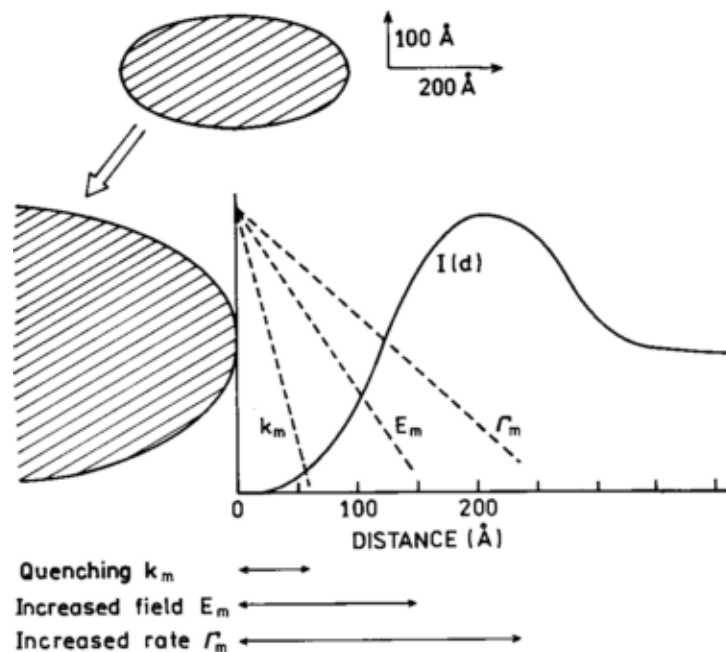
Figure 8: An intensity of a fluorophore as a function of fluorophore-NP distance d.[96] Increased emission intensity is observed approximately 20 nm from NP surface. Small distances lead to minor emission and quenching of the fluorescence. With long distances the fluorescence intensity is unaffected.

2.3.4 Engineering of the complex enhances the fluorescence properties

After going through the theory, one can summarise that the fluorescence properties of AgNP-CBDmon complex may be modified by numerous different ways. Tuning of the LSPR wavelength, the length of the ligand and/or the structure of CBDmon may be done and they all have a potential effect to the final radiative properties.

Engineering of the complex may be done by choosing an appropriate ligand between NP and fluorophore which acts as an insulating layer in synthesized complex. MEF is through-space interaction and careful tuning of the NP-fluorophore distance can increase the intensity of the fluorophore.[91, 96, 100] (Fig. 8) The possibility of quenching increases when the fluorophore is close to the particle surface or other fluorescent molecule.[33, 91, 101] For example, the studies with green fluorescent protein indicate that close packing of proteins on the surface may allow self-quenching by ET.[102] ET may also occur between NP and fluorophore when the energy is dis-

sipated into the absorption of LSPR in metal.[96] However, if the distance is tuned properly NPs are proved to lower the propability of self-quenching.[101]

Engineering the size, shape and material of the NPs determine the properties of LSPR which are important to make overlap with fluorophore's excitation and/or emission spectra.[33,82] The interactions occur only on the energy scale of the absorbed photon and thus the fluorophore absorption and/or excitation may be enhanced only near the wavelengths of LSPR.[82] It is also important to balance the absorptive and scattering natures of the AgNPs as the dominative nature of absorption leads to plasmonic losses in the metal and scattering to radiation of photons in the LSPR wavelength.[34,92] With different combinations of size and material the wavelength of the LSPR can be tuned into almost anywhere in visible wavelengths.[34,71] The highest brightness is obtained when LSPR is between absorption and emission and NPs enhance emission of the fluorophore.[82]

3   Experimental methods, Results and Discussion

Experimental methods, sample preparation, results and discussion are described in the Article which can be found as the Appendix 2.

4   Concluding Remarks and Future Perspectives

In this Thesis it is shown that the photochemical properties of CBDmon can be modified with AgNPs. CBDmons and AgNPs can be successfully attached to each other with BCML-molecules and the synthesis is repeatable. The formation of the complex induced also distinct enhancements to QY and brightness. Thus, all the aims of the project were achieved. However, engineering of the AgNP-CBDmon complex could be made further and thus some promising improvements are described.

(I) Tuning of the size, shape and material of NPs. Engineering of these properties decide the wavelength of LSPR. In this Thesis, the wavelength was fixed into Soret band of CBDmon which gave the possibility to study the changes in the fluorescence properties of AgNP-CBDmon complex but also the changes in

CBDmon photoconversion. However, the synthesized complex was not ideal for the viewpoint of enhancement and thus QY and brightness may be improved by even higher factors. According to the literature, the highest enhancements are acquired when the LSPR peak overlaps both absorption and emission spectra.[82] LSPR was focused only into absorption band and thus only absorption of CBDmon was enhanced. This yielded only minor improvement for QY, but higher enhancement for brightness if excited from the Soret band. Thus, moving the LSPR between Q-band and fluorescence would likely tune QY and brightness into the highest values. To obtain the proper LSPR wavelength, one could use, e.g., silver nanotriangles[68] or different shapes of gold NPs.[103,104]

(II) Utilizing the local enhanced electric fields. After the LSPR wavelength is tuned, one has still possibilities to improve the emission from the chromophore. It is known that anisotropy of the metallic NP focuses the plasmonic electric fields into smaller areas[105] or the enhanced electric fields can be induced between two plasmonic NPs.[106] These local fields are called hot spots and they are used successfully in applications where, e.g., bowties enhance the fluorescence[107] or fluorescein is placed between metallic NPs.[108,22] In all these applications, fluorescence is increased more than in the case of single NPs. Thus, utilizing the hotspots might be a promising direction to the engineering and provide additional enhancements for QY and brightness.

(III) Selection of biomaterial. During the engineering of the emission it is important to notice that advancement occurs also on the field of fluorophores. Better fluorescent properties from the beginning improve the absolute amount of photons acquired from the label. For example, CBD has mutations which have higher QY[10,13] and also other promising phytochromes are developed.[15] Thus, it is reasonable to search and use the best biomaterial available which is suitable for the needs.

(IV) Selection of the ligand. Tuning of the ligand seems a fine adjustment to the complex, but it has an effect for the emission intensity. The ligand decides the distance between the NP and fluorophores which was not tuned in this Thesis. Therefore, the change of the BCML to something else would have a potential to improve QY and brightness of the complex. However, when BCML is changed

one has to ensure the binding ability to the biomaterial, e.g. CBDmon. Thus, mastering the synthesis of the complex with new ligand would be a task for a new project because it requires more time.

References

1. M. S. T. Goncalves. Fluorescent Labeling of Biomolecules with Organic Probes. *Chemical Reviews*, 109:190–212, 2009.

2. U. Resch-Genger, M. Grabolle, S. Cavaliere-Jaricot, R. Nitschke, and T. Nann. Quantum dots versus organic dyes as fluorescent labels. *Nature methods*, 5:763–775, 2008.

3. S. Luo, E. Zhang, Y. Su, T. Cheng, and C. Shi. A review of NIR dyes in cancer targeting and imaging. *Biomaterials*, 32:7127–7138, 2011.

4. M. J. Ruedas-Rama, J. D. Walters, A. Orte, and E. A. H. Hall. Fluorescent nanoparticles for intracellular sensing: A review. *Analytica Chimica Acta*, 751:1–23, 2012.

5. A. M. Smith, M. C. Mancini, and S. Nie. Second Window for In Vivo Imaging. *Nature Nanotechnology*, 4:710–711, 2009.

6. J Zhang, R E Campbell, A Y Ting, and R Tsien. Creating new fluorescent probes for cell biology. *Nature Reviews Molecular Cell Biology*, 3(12):906–918, 2002.

7. M. Zimmer. Green fluorescent protein (GFP): Applications, structure, and related photophysical behavior. *Chemical Reviews*, 102:759–781, 2002.

8. R. E. Campbell, O. Tour, A. E. Palmer, P. A. Steinbach, G. S. Baird, D. A. Zacharias, and R. Y. Tsien. A monomeric red fluorescent protein. *Proceedings of the National Academy of Sciences of the United States of America*, 99:7877–82, 2002.

9. T. Nagai, K. Ibata, E. S. Park, M. Kubota, K. Mikoshiba, and A. Miyawaki. A variant of yellow fluorescent protein with fast and efficient maturation for cell-biological applications. *Nature biotechnology*, 20:87–90, 2002.

10. H. Lehtivuori, S. Bhattacharya, N. M. Angenent-Mari, K. A. Satyshur, and K. T. Forest. Removal of Chromophore-Proximal Polar Atoms Decreases Water Content and Increases Fluorescence in a Near Infrared Phytofluor. *Frontiers in Molecular Biosciences*, 2, 2015.

11. M.E. Auldridge, K. A. Satyshur, D. M. Anstrom, and K. T. Forest. Structure-guided engineering enhances a phytochrome-based infrared fluorescent protein. *Journal of Biological Chemistry*, 287:7000–7009, 2012.

12. S. Bhattacharya, M.E. Auldridge, H. Lehtivuori, J. Ihalainen, and K. Forest. Origins of Fluorescence in Evolved Bacteriophytochromes. *J. Biol. Chem.*, 289:32144–32152, 2014.

13. D. Yu, W. C. Gustafson, C. Han, C. Lafaye, M. Noirclerc-Savoye, W. Ge, D. A. Thayer, H. Huang, T. B. Kornberg, A. Royant, L. Y. Jan, Y. N. Jan, W. A. Weiss, and X. Shu. An improved monomeric infrared fluorescent protein for neuronal and tumour brain imaging. *Nature Communications*, 5:3626, 2014.

14. G. S. Filonov, K. D. Piatkevich, L. M. Ting, J. Zhang, K. Kim, and V. V. Verkhusha. Bright and stable near-infrared fluorescent protein for in vivo imaging. *Nat Biotechnol*, 29:757–761, 2011.

15. D. M. Shcherbakova and V. V. Verkhusha. Near-infrared fluorescent proteins for multicolor in vivo imaging. *Nature methods*, 10:751–754, 2013.

16. H Smith. Phytochromes and light signal perception by plants–an emerging synthesis. *Nature*, 407:585–591, 2000.

17. S.J. Davis, A.V. Vener, and R.D. Vierstra. Bacteriophytochromes: Phytochrome-Like Photoreceptors from Nonphotosynthetic Eubacteria. *Science*, 286:2517–2520, 1999.

18. J. R. Wagner, J. Zhang, J. S. Brunzelle, R. D. Vierstra, and K. T. Forest. High resolution structure of Deinococcus bacteriophytochrome yields new insights into phytochrome architecture and evolution. *Journal of Biological Chemistry*, 282:12298–12309, 2007.

19. X. Shu, A. Royant, M. Z. Lin, T. A. Aguilera, V. Lev-Ram, P. A. Steinbach, and R. Y. Tsien. Mammalian Expression of Infrared Fluorescent Proteins Engineered from a Bacterial Phytochrome. *Science*, 324:804–807, 2009.

20. J. A. Ihalainen, H. Takala, and H. Lehtivuori. Fast Photochemistry of Proto-typical Phytochromes—A Species vs. Subunit Specific Comparison. *Frontiers in Molecular Biosciences*, 2, 2015.

21. J. R. Wagner, J. S. Brunzelle, K. T. Forest, and R. D. Vierstra. A light-sensing knot revealed by the structure of the chromophore-binding domain of phytochrome. *Nature*, 438:325–331, 2005.

22. J. Zhang, Y. Fu, M. H. Chowdhury, and J. R. Lakowicz. Metal-enhanced single-molecule fluorescence on silver particle monomer and dimer: Coupling effect between metal particles. *Nano Letters*, 7:2101–2107, 2007.

23. Y-Q. Li, L-Y. Guan, H-L. Zhang, J. Chen, S. Lin, Z-Y. Ma, and Y-D. Zhao. Distance-Dependent Metal-Enhanced Quantum Dots Fluorescence Analysis in Solution by Capillary Electrophoresis and Its Application to DNA Detection. | *Anal. Chem*, 83:4103–4109, 2011.

24. Y. Fu, J. Zhang, and J. R. Lakowicz. Metal-enhanced fluorescence of single green fluorescent protein (GFP). *Biochemical and Biophysical Research Communications*, 376:712–717, 2008.

25. K. Aslan, I. Gryczynski, J. Malicka, E. Matveeva, J.R. Lakowicz, and C.D. Geddes. Metal-enhanced fluorescence: An emerging tool in biotechnology, 2005.

26. J. Zhang, J. Malicka, I. Gryczynski, and J. R. Lakowicz. Oligonucleotide-displaced organic monolayer-protected silver nanoparticles and enhanced lu-

minescence of their salted aggregates. *Analytical Biochemistry*, 330:81–86, 2004.

27. K. Aslan, J. R. Lakowicz, H. Szmacinski, and C. D. Geddes. Metal-enhanced fluorescence solution-based sensing platform. *Journal of Fluorescence*, 14:677–679, 2004.

28. J. Malicka, I. Gryczynski, C. D. Geddes, and J. R. Lakowicz. Metal-enhanced emission from indocyanine green: a new approach to in vivo imaging. *Journal of Biomedical Optics*, 8:472–478, 2003.

29. I. Gryczynski, J. Malicka, E. Holder, N. DiCesare, and J. R. Lakowicz. Effects of metallic silver particles on the emission properties of [Ru(bpy)3]2+. *Chemical Physics Letters*, 372:409–414, 2003.

30. C. D. Geddes, H. Cao, I. Gryczynski, Z. Gryczynski, J. Fang, and J. R. Lakowicz. Metal-enhanced fluorescence (MEF) due to silver colloids on a planar surface: Potential applications of indocyanine green to in vivo imaging. *Journal of Physical Chemistry A*, 107:3443–3449, 2003.

31. P C Lee and D Meisel. Adsorption and surface-enhanced Raman of dyes on silver and gold sols. *J.Phys.Chem.*, 86:3391–3395, 1982.

32. M. Ahamed, M. S. Alsalhi, and M. K. J. Siddiqui. Silver nanoparticle applications and human health. *Clinica Chimica Acta*, 411:1841–1848, 2010.

33. E. Petryayeva and U. J. Krull. Localized surface plasmon resonance: Nanostructures, bioassays and biosensing-A review. *Analytica Chimica Acta*, 706:8–24, 2011.

34. S. Maier. *Plasmonics : Fundamentals and Applications*. Springer, 2007.

35. W. L. Barnes, A. Dereux, and T. W. Ebbesen. Surface plamons subwavelength optics. *Nature*, 424:824–830, 2003.

36. J. R. Lakowicz. *Principles of Fluorescence Spectroscopy*. Springer, 3rd edition, 2006.

37. S. H. Bhoo, S. J. Davis, J. Walker, B. Karniol, and R. D. Vierstra. Bacteriophytochromes are photochromic histidine kinases using a biliverdin chromophore. *Nature*, 414:776–779, 2001.

38. A. F. McDonagh and L. A. Palma. Preparation and Properties of Crystalline Biliverdin IXalpha. *Biochemistry Journal*, 189:193–208, 1980.

39. J. R. Wagner, J. Zhang, D. Von Stetten, M. Günther, D. H. Murgida, M. A. Mroginski, J. M. Walker, K. T. Forest, P. Hildebrandt, and R. D. Vierstra. Mutational analysis of Deinococcus radiodurans bacteriophytochrome reveals key amino acids necessary for the photochromicity and proton exchange cycle of phytochromes. *Journal of Biological Chemistry*, 283:12212–12226, 2008.

40. C. Song, T. Rohmer, M. Tiersch, J. Zaanen, J. Hughes, and J. Org Matysik. Solid-State NMR Spectroscopy to Probe Photoactivation in Canonical Phytochromes. *Photochemistry and Photobiology*, 89:259–273, 2013.

41. H. Falk. *The Chemistry of Linear Oligopyrroles and Bile Pigments*. Springer Vienna, 1989.

42. K. M. Kadish, K. M. Smith, and R. Guilard. *Handbook of porphyrin science : with applications to chemistry, physics, materials science, engineering, biology and medicine.* World Scientific, 2010.

43. J. M. Dixon, M. Taniguchi, and J. S. Lindsey. Software Note PhotochemCAD 2: A Refined Program with Accompanying Spectral Databases for Photochemical Calculations. *Photochemistry and Photobiology*, 81:212–213, 2005.

44. H. Takala, A. Björling, M. Linna, S. Westenhoff, and J. A. Ihalainen. Light-induced changes in the dimerization interface of bacteriophytochromes. *Journal of Biological Chemistry*, 290:16383–16392, 2015.

45. D. Von Stetten, S. Seibeck, N. Michael, P. Scheerer, M. A. Mroginski, D. H. Murgida, N. Krauss, M. P. Heyn, P. Hildebrandt, B. Borucki, and T. Lamparter. Highly conserved residues Asp-197 and His-250 in Agp1 phytochrome control the proton affinity of the chromophore and Pfr formation. *Journal of Biological Chemistry*, 282:2116–2123, 2007.

46. B. Borucki, D. Von Stetten, S. Seibeck, T. Lamparter, N. Michael, M. A. Mroginski, H. Otto, D. H. Murgida, M. P. Heyn, and P. Hildebrandt. Light-induced proton release of phytochrome is coupled to the transient deprotonation of the tetrapyrrole chromophore. *Journal of Biological Chemistry*, 280:34358–34364, 2005.

47. M. Feliks, C. Lafaye, X. Shu, A. Royant, and M. Field. Structural Determinants of Improved Fluorescence in a Family of Bacteriophytochrome-Based Infrared Fluorescent Proteins: Insights from Continuum Electrostatic Calculations and Molecular Dynamics Simulations. *Biochemistry*, 55:4263–4274, 2016.

48. Nathan C Rockwell, Yi-Shin Su, and J Clark Lagarias. Phytochrome Structure and Signaling Mechanisms. *Annual Review of Plant Biology*, 57:837–858, 2006.

49. K. C. Toh, E. A. Stojkovic, I. H. M. van Stokkum, K. Moffat, and J. T. M. Kennis. Proton-transfer and hydrogen-bond interactions determine fluorescence quantum yield and photochemical efficiency of bacteriophytochrome. *Proceedings of the National Academy of Sciences*, 107:9170–9175, 2010.

50. M. Kasha. Characterization of electronic transitions in complex molecules. *Discussions of the Faraday Society*, 9:14, 1950.

51. P. W. Atkins and J. De Paula. *Physical chemistry*. W.H. Freeman and Co, 9th edition, 2010.

52. Y. Tian, J. Halle, M. Wojdyr, Di. Sahoo, and I. G. Scheblykin. Quantitative measurement of fluorescence brightness of single molecules. *Methods and Applications in Fluorescence*, 2, 2014.

53. C. Würth, M. Grabolle, J. Pauli, M. Spieles, and U. Resch-genger. Relative and absolute determination of fluorescence quantum yields of transparent samples. *Nature protocols*, 8(8):1535–50, 2013.

54. T. Rohmer, C. Lang, C. Bongards, K. B. S. S. Gupta, J. Neugebauer, J. Hughes, W. Gärtner, and J. Matysik. Phytochrome as molecular machine: Revealing chromophore action during the Pfr → Pr photoconversion by magic-angle spinning NMR spectroscopy. *Journal of the American Chemical Society*, 132:4431–4437, 2010.

55. H. Takala, A. Björling, . Berntsson, H. Lehtivuori, S. Niebling, M. Hoernke, I. Kosheleva, R. Henning, A. Menzel, J. A. Ihalainen, and S. Westenhoff. Signal amplification and transduction in phytochrome photosensors. *Nature*, 509:245–248, 2014.

56. P. Eilfeld and Olfhart R. W. Absorption Spectra of Phytochrome Intermediates. *Z. Naturforsch*, 40 c:109–114, 1985.

57. T. Mathes, J. Ravensbergen, M. Kloz, T. Gleichmann, K. D. Gallagher, N. C. Woitowich, R. St. Peter, S. E. Kovaleva, E. A. Stojković, and J. T.M. Kennis. Femto- to Microsecond Photodynamics of an Unusual Bacteriophytochrome. *Journal of Physical Chemistry Letters*, 6:239–243, 2015.

58. R. Berera, R. van Grondelle, and J. T. M. Kennis. Ultrafast transient absorption spectroscopy: Principles and application to photosynthetic systems. *Photosynthesis Research*, 101:105–118, 2009.

59. N. V. Tkachenko. *Optical spectroscopy : methods and instrumentations*. Elsevier, 2006.

60. I. H.M. van Stokkum, D. S. Larsen, and R. van Grondelle. Global and target analysis of time-resolved spectra. *Biochimica et Biophysica Acta - Bioenergetics*, 1657:82–104, 2004.

61. M. A. Mroginski, D. H. Murgida, and P. Hildebrandt. The chromophore structural changes during the photocycle of phytochrome: A combined resonance Raman and quantum chemical approach. *Accounts of Chemical Research*, 40:258–266, 2007.

62. W. Becker. *Advanced time-correlated single photon counting techniques*. Springer, 2005.

63. D.V. O'Connor, W.R. Ware, and J.C. Andre. Deconvolution of Fluorescence Decay Curves. A Critical Comparison of techniques. *The Journal of Physical Chemistry*, 83:1333–1343, 1979.

64. E. Fort and S. Gresillon. Surface enhanced fluorescence. *Journal of Physics D-Applied Physics*, 41:31, 2008.

65. G. V. Naik, V. M. Shalaev, and A. Boltasseva. Alternative plasmonic materials: Beyond gold and silver, 2013.

66. K. S. Lee and M. A. El-Sayed. Gold and silver nanoparticles in sensing and imaging: Sensitivity of plasmon response to size, shape, and metal composition. *Journal of Physical Chemistry B*, 110:19220–19225, 2006.

67. S. Link, Z. L. Wang, and M. A. El-Sayed. Alloy Formation of Gold-Silver Nanoparticles and the Dependence of the Plasmon Absorption on Their Composition. *The Journal of Physical Chemistry B*, 103:3529–3533, 1999.

68. J. N. Anker, W. P. Hall, O. Lyandres, N. C. Shah, J. Zhao, and R. P. Van Duyne. Biosensing with plasmic nanostructure. *Nature methods*, 7:442–453, 2008.

69. D. Paramelle, A. Sadovoy, S. Gorelik, P. Free, J. Hobley, and D. G. Fernig. A rapid method to estimate the concentration of citrate capped silver nanoparticles from UV-visible light spectra. *The Analyst*, 139:4855–61, 2014.

70. C. F. Bohren and D. R. Huffman. *Absorption and Scattering of Light by Small Particles*. John Wiley & Sons, Inc., New York, 1st edition, 1983.

71. J. R. Lakowicz. Plasmonics in biology and plasmon-controlled fluorescence. *Plasmonics*, 1:5–33, 2006.

72. W L Barnes. Fluorescence near interfaces: the role of photonic mode density. 45:661–699, 1998.

73. D. R. Bae, W. S. Han, J. M. Lim, S. Kang, J. Y. Lee, D. Kang, and J. H. Jung. Lysine-Functionalized Silver Nanoparticles for Visual Detection and

Separation of Histidine and Histidine-Tagged Proteins. *Langmuir*, 26:2181–2185, 2010.

74. L. Nuuttila, K. Tapio, T. Lemma, J. A. Ihalainen, N.V. Tkachenko, J. J. Toppari, and H. Lehtivuori. Enhancing fluorescence of monomeric bacterio-phytochromes by plasmonic nanoparticles. *Submitted*, 2017.

75. M. E. Peskin and D. V. Schroeder. *An introduction to quantum field theory.* Westview press, 1995.

76. P. Törmä and W. L. Barnes. Strong coupling between surface plasmon polaritons and emitters: a review. *Reports on progress in physics. Physical Society (Great Britain)*, 78:013901, 2015.

77. J. Kasprzak, M. Richard, S. Kundermann, A. Baas, P. Jeambrun, J. M. J. Keeling, F. M. Marchetti, M. H. Szymańska, R. André, J. L. Staehli, V. Savona, P. B. Littlewood, B. Deveaud, and Le. Si. Dang. Bose-Einstein condensation of exciton polaritons. *Nature*, 443:409–414, 2006.

78. J. A. Hutchison, T. Schwartz, C. Genet, E. Devaux, and T. W. Ebbesen. Modifying chemical landscapes by coupling to vacuum fields. *Angewandte Chemie - International Edition*, 51:1592–1596, 2012.

79. P.R. Rice and H.J. Carmichael. Photon statistics of a Cavity-QED Laser: a Comment on the Laser-Phase-Transition Analogy. *Phys. Rev. A*, 50:4318–4329, 1994.

80. E. Matveeva, Z. Gryczynski, J. Malicka, I. Gryczynski, and J. R. Lakowicz. Metal-enhanced fluorescence immunoassays using total internal reflection and silver island-coated surfaces. *Analytical Biochemistry*, 334:303–311, 2004.

81. J. R. Lakowicz, J. Malicka, and I. Gryczynski. Silver particles enhance emission of fluorescent DNA oligomers. *BioTechniques*, 34:62–68, 2003.

82. Y. Chen, K. Munechika, and D. S. Ginger. Dependence of fluorescence intensity on the spectral overlap between fluorophores and plasmon resonant single silver nanoparticles. *Nano Letters*, 7:690–696, 2007.

83. A. J. Haes, D. A. Stuart, S. Nie, and R. P. Van Duyne. Using solution-phase nanoparticles, surface-confined nanoparticle arrays and single nanoparticles as biological sensing platforms, 2004.

84. A. J. Haes, L. Chang, W. L. Klein, and R. P. Van Duyne. Detection of a biomarker for Alzheimer's disease from synthetic and clinical samples using a nanoscale optical biosensor. *Journal of the American Chemical Society*, 127:2264–2271, 2005.

85. M. P. Kreuzer, R. Quidant, J. P. Salvador, M. P. Marco, and G. Badenes. Colloidal-based localized surface plasmon resonance (LSPR) biosensor for the quantitative determination of stanozolol. *Analytical and Bioanalytical Chemistry*, 391:1813–1820, 2008.

86. A. J. Haes, S. Zou, G. C. Schatz, and R. P. Van Duyne. Nanoscale Optical Biosensor: Long Range Distance Dependence of the Localized Surface Plasmon Resonance of Noble Metal Nanoparticles. *The Journal of Physical Chemistry B*, 108:109–116, 2004.

87. A. J. Haes, S. Zou, G. C. Schatz, and R. P. Van Duyne. Nanoscale optical biosensor: Short range distance dependence of the localized surface plasmon resonance of noble metal nanoparticles. *The Journal of Physical Chemistry B*, 108:6961–6968, 2004.

88. A. V. Whitney, J. W. Elam, S. Zou, A. V. Zinovev, P. C. Stair, G. C. Schatz, and R. P. Van Duyne. Localized surface plasmon resonance nanosensor: a high-resolution distance-dependence study using atomic layer deposition. *The journal of physical chemistry. B*, 109:20522–20528, 2005.

89. K. A. Willets and R. P. Van Duyne. Localized Surface Plasmon Resonance Spectroscopy and Sensing. *The annual review of physical chemistry*, 58:267–297, 2007.

90. A. J. Haes, S. Zou, J. Zhao, G. C. Schatz, and R. P. Van Duyne. Localized surface plasmon resonance spectroscopy near molecular resonances. *Journal of the American Chemical Society*, 128:10905–10914, 2006.

91. J. R. Lakowicz, J. Malicka, I. Gryczynski, Z. Gryczynski, and C. D. Geddes. Radiative decay engineering: the role of photonic mode density in biotechnology. *Journal of physics D: Applied physics*, 36:R240–R249, 2003.

92. J. R. Lakowicz. Radiative decay engineering: 5. Metal-enhanced fluorescence and plasmon emission. *Analytical Biochemistry*, 337:171–194, 2005.

93. O. Andreussi, S. Corni, B. Mennucci, and J. Tomasi. Radiative and nonradiative decay rates of a molecule close to a metal particle of complex shape. *Journal of Chemical Physics*, 121:10190–10202, 2004.

94. R. Carminati, J. J. Greffet, C. Henkel, and J. M. Vigoureux. Radiative and non-radiative decay of a single molecule close to a metallic nanoparticle. *Optics Communications*, 261:368–375, 2006.

95. J. R. Lakowicz, C. D. Geddes, I. Gryczynski, J. Malicka, Z. Gryczynski, K. Aslan, J. Lukomska, E. Matveeva, J. Zhang, R. Badugu, and J. Huang. Advances in Surface-Enhanced Fluorescence. *Journal of F*, 14:425–441, 2004.

96. J R Lakowicz. Radiative decay engineering: 1. biophysical and biomedical applications. *Analytical biochemistry*, 298:1–24, 2001.

97. E. Dulkeith, A. C. Morteani, T. Niedereichholz, T. A. Klar, J. Feldmann, S. A. Levi, F. C. J. M. van Veggel, D. N. Reinhoudt, M. Möller, and D. I. Gittins. Fluorescence quenching of dye molecules near gold nanoparticles: radiative and nonradiative effects. *Physical review letters*, 89:203002, 2002.

98. W. Trabesinger, A. Kramer, M. Kreiter, B. Hecht, and U. P. Wild. Single-molecule near-field optical energy transfer microscopy Optical near-field enhancement at a metal tip probed by a single fluorophore Scanning near-field optical microscopy with aperture probes: Fundamentals and applications Single-molecule near-fiel. *Appl. Phys. Lett.*, 81:2118–2120, 2002.

99. E. Dulkeith, M. Ringler, T. A. Klar, J. Feldmann, A. Javier Muñoz, and W. J. Parak. Gold nanoparticles quench fluorescence by phase induced radiative rate suppression. *Nano Letters*, 5:585–589, 2005.
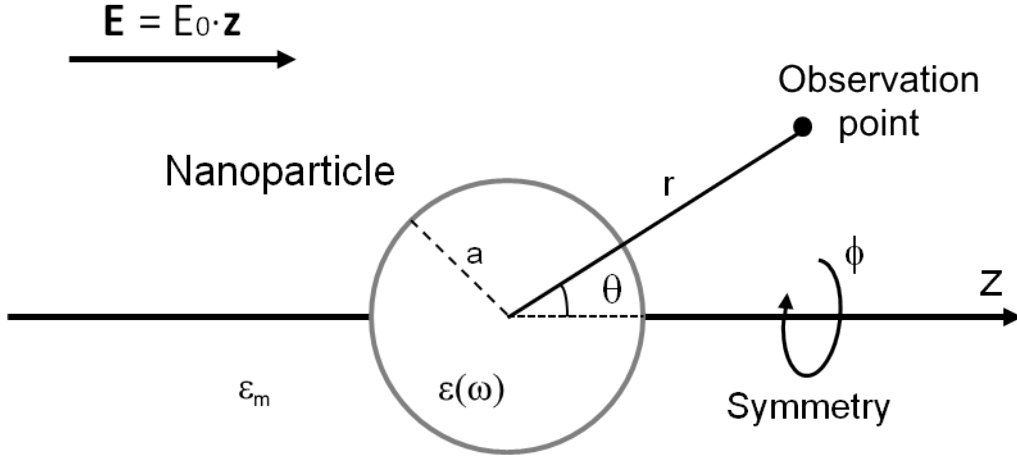
100. P. Anger, P. Bharadwaj, and L. Novotny. Enhancement and quenching of single-molecule fluorescence. *Physical Review Letters*, 96:3–6, 2006.

101. J. R. Lakowicz, J. Malicka, S. D'Auria, and I. Gryczynski. Release of the self-quenching of fluorescence near silver metallic surfaces. *Analytical Biochemistry*, 320:13–20, 2003.

102. G. H. Patterson, D. W. Piston, and B. G. Barisas. Förster Distances between Green Fluorescent Protein Pairs. *Analytical Biochemistry*, 284:438–440, 2000.

103. H. Chen, X. Kou, Z. Yang, W. Ni, and J. Wang. Shape- and size-dependent refractive index sensitivity of gold nanoparticles. *Langmuir*, 24:5233–5237, 2008.

104. L. Scarabelli, M. Coronado-Puchau, J. J. Giner-Casares, J. Langer, and L. M. Liz-Marzán. Monodisperse gold nanotriangles: Size control, large-scale self-assembly, and performance in surface-enhanced raman scattering. *ACS Nano*, 8:5833–5842, 2014.

105. K. B. Crozier, A. Sundaramurthy, G. S. Kino, and C. F. Quate. Optical antennas: Resonators for local field enhancement. *Journal of Applied Physics*, 94:4632–4642, 2003.

106. R. Hillenbrand and F. Keilmann. Optical oscillation modes of plasmon particles observed in direct space by phase-contrast near-field microscopy. *Applied Physics B: Lasers and Optics*, 73:239–243, 2001.

107. A. Kinkhabwala, Z. Yu, S. Fan, Y. Avlasevich, K. Müllen, and W. E. Moerner. Large single-molecule fluorescence enhancements produced by a bowtie nanoantenna. *Nature Photonics*, 3:654–657, 2009.

108. A. Bek, R. Jansen, M. Ringler, S. Mayilo, T. A. Klar, and J. Feldmann. Fluorescence enhancement in hot spots of AFM-designed gold nanoparticle sandwiches. *Nano Letters*, 8:485–490, 2008.

Appendix

Figure 1: A silver nanoparticle with dielectric constant ε inserted into a constant electric field $\overline{E}$ in a surrounding medium (with electric constant ε_m). The particle has radius a and it is located in the z-axis. The cylindrical symmetry gives identical electrostatic potential to every point with same ϕ which reduces the problem into two dimensions (r,θ). Edited from Maier.[1]

Polarizability of Metal Nanoparticles

This appendix reviews a derivation to the polarizability (α) of a spherical metal nanoparticle (NP) when a quasi-static approximation can be applied. A simple approach to demonstrate the phenomenon is to use the classical methods for spherical NPs and study the electric potential Φ in the vicinity of the NP.[1,2] α can be further derived from Φ and it is used to the determination of LSPR conditions.

Inserting a NP into the visible light (380-800 nm)[3,4] will give a situation where the diameter of the NP (d_{NP}) is much smaller than the wavelength of the incident light (λ_{light}). When the condition $d_{NP} \ll \lambda_{light}$ is fulfilled the electric field on the vicinity of the NP is nearly constant and thus it can be treated as constant electric field. This is called a quasi-static approximation and it allows the classical analysis to Φ in and outside the particle.[1]

As shown in Figure 1, the approximation states that the electric field of the light is constant near the NP and it is form of $\overline{E} = E_0\widehat{z}$ where $\widehat{z}$ is the direction perpendicular to the proceeding light. To calculate the electrostatic potential Φ, the Laplacian equation $\Delta^2\Phi = 0$ can be utilised. Due to the spherical shape of the

particle, observation point has now axial symmetry in any azimutal angle ϕ. As a conductor, silver has free charges distributed only on the surface of the sphere. Electrostatic potential in observation point has now general solutions[2] inside the sphere

$$\Phi_{in}(r,\theta) = \Sigma_{l=0}^{\infty} A_l r^l P_l\left(\cos\theta\right) \tag{1}$$

and outside the sphere

$$\Phi_{out}(r,\theta) = \Sigma_{l=0}^{\infty}[B_l r^l + C_l r^{-(l+1)}]P_l\left(\cos\theta\right), \tag{2}$$

where A_l, B_l and C_l are coefficients and $P_l(cos\theta)$ Legendre polynomials of lth order.

B_l can be determined by using boundary conditions far from sphere $(r \to \infty)$ whereas A_l and C_l are obtained using the conditions at the surface $(r = a)$ where the equation of the electrostatic potential changes.[1,2] Far from the sphere the electric field recovers back to $\overline{E} = E_0\widehat{z}$ and the electric potential in the observation point is $-E_0 z$. Conversion to spherical coordinates gives a boundary condition which states

$$\Phi_{out}(r, \theta)\Big|_{r=\infty} = -E_0 r \cos\theta. \tag{3}$$

From the equation (2) can be seen that $r^l = r$ only when $l = 1$ and $r^{-(l+1)} \to 0$, $\forall\, l \in [0,\infty[$ when r increases. Leaving Φ_{out} to the form

$$\Phi_{out}(r, \theta) = B_1 r P_1(\cos\theta) = B_1 r \cos\theta, \tag{4}$$

where $P_1(\cos\theta) = \cos\theta$.[2] Equality with the equation (3) now gives $B_1 = -E_0$ while other terms in Φ_{out} vanish.

Coefficients A_l and C_l are determined from the boundary conditions on the sphere surface. Internal and external electric fields $(\overline{E} = -\nabla\Phi)$ match on the surface which yields equality

$$-\frac{1}{a}\frac{\partial\Phi_{in}}{\partial\theta}\Big|_{r=a} = -\frac{1}{a}\frac{\partial\Phi_{out}}{\partial\theta}\Big|_{r=a} \tag{5}$$

to tangential direction in the spherical coordinates. Similarly the internal and

external displacement fields ($\overline{D} = \varepsilon_0 \varepsilon \overline{E}$) match on the surface and give the equality

$$- \varepsilon_0 \varepsilon \frac{\partial \Phi_{in}}{\partial r}\bigg|_{r=a} = -\varepsilon_0 \varepsilon_m \frac{\partial \Phi_{out}}{\partial r}\bigg|_{r=a} \tag{6}$$

to the normal direction, where ε_0 is the electric permittivity and ε or ε_m are dielectric constants of the metal or medium. Substituting equations (1) and (2) to (5) and (6) will give equations

$$-\frac{1}{a} \cdot \frac{\partial}{\partial \theta} \left(\Sigma_{l=0}^{\infty} A_l r^l P_l(\cos \theta) - \Sigma_{l=0}^{\infty} C_l r^{-(l+1)} P_l(\cos \theta) + E_0 r \cos \theta \right)\bigg|_{r=a} = 0 \quad (7)$$

and

$$- \varepsilon_0 \frac{\partial}{\partial r} \left(\varepsilon \Sigma_{l=0}^{\infty} A_l r^l P_l(\cos \theta) - \varepsilon_m \Sigma_{l=0}^{\infty} C_l r^{-(l+1)} P_l(\cos \theta) + \varepsilon_m E_0 r \cos \theta \right)\bigg|_{r=a} = 0. \tag{8}$$

These equations can be simplified to forms

$$-\frac{1}{a} \left(\Sigma_{l=0}^{\infty} A_l a^l P_l^1 - \Sigma_{l=0}^{\infty} C_l a^{-(l+1)} P_l^1 + E_0 a \sin \theta \right) = 0 \tag{9}$$

and

$$-\varepsilon_0 (\varepsilon \Sigma_{l=0}^{\infty} A_l l a^{l-1} P_l + \varepsilon_m \Sigma_{l=0}^{\infty} C_l (l+1) a^{-(l+2)} P_l + \varepsilon_m E_0 \cos \theta) = 0, \tag{10}$$

where $P_l^1 = \partial P_l / \partial \theta$ and $P_l = P_l(\cos\theta)$ behave as constants due to the orthogonality to the normal vector.[2] Because $\sin \theta$ and $\cos \theta$ can have nonzero values, the series equal zero only if

$$-\frac{1}{a} \left(\Sigma_{l=0}^{\infty} A_l a^l P_l^1 - \Sigma_{l=0}^{\infty} C_l a^{-(l+1)} P_l^1 + E_0 a \right) = 0 \tag{11}$$

and

$$- \varepsilon_0 \left(\varepsilon \Sigma_{l=0}^{\infty} A_l l a^{l-1} P_l + \varepsilon_m \Sigma_{l=0}^{\infty} C_l (l+1) a^{-(l+2)} P_l + \varepsilon_m E_0 \right) = 0, \tag{12}$$

where all the lth terms vanish separately. Vanishing conditions can be separated for $l \neq 1$ and $l = 1$ of which the latter has easily solved coefficients. When $l \neq 1$ the general solutions are

$$A_l = \frac{C_l}{a^{2l+1}} \tag{13}$$

and

$$A_l = -\frac{l+1}{l}\frac{\varepsilon_m}{\varepsilon}\frac{C_l}{a^{2l+1}}, \tag{14}$$

which are satisfied only with $A_l = C_l = 0$. This gives no terms for coefficients. For $l = 1$ the solutions are

$$A_1 = -E_0 + \frac{C_1}{a^3} \tag{15}$$

and

$$A_1 = \frac{\varepsilon_m}{\varepsilon}\left(-E_0 - 2\frac{C_1}{a^3}\right). \tag{16}$$

Substituting equation (15) into equation (16) the coefficients become

$$C_1 = \frac{\frac{\varepsilon_m}{\varepsilon} - 1}{-2\frac{\varepsilon_m}{\varepsilon} - 1}a^3 E_0 = \frac{\varepsilon_m - \varepsilon}{\varepsilon + 2\varepsilon_m}a^3 E_0 \tag{17}$$

and

$$A_1 = -E_0 + \frac{1}{a^3}\frac{\varepsilon - \varepsilon_m}{\varepsilon + 2\varepsilon_m}a^3 E_0 = -E_0\frac{3\varepsilon_m}{\varepsilon + 2\varepsilon_m}. \tag{18}$$

Inserting the calculated A_l, B_l and C_l into equations (1) and (2) the electrostatic potential has the final forms of

$$\Phi_{in} = -\frac{3\varepsilon_m}{\varepsilon + 2\varepsilon_m}E_0 r\cos\theta \tag{19}$$

and

$$\begin{aligned}\Phi_{out} &= -E_0 r cos\theta + \frac{\varepsilon - \varepsilon_m}{\varepsilon + 2\varepsilon_m}E_0 a^3\frac{\cos\theta}{r^2} \\ &= -E_0 r cos\theta + \alpha E_0\frac{\cos\theta}{4\pi r^2},\end{aligned} \tag{20}$$

where α is the polarizability of the NP

$$\alpha = 4\pi a^3\frac{\varepsilon - \varepsilon_m}{\varepsilon + 2\varepsilon_m}. \tag{21}$$

A closer look at the equation (21) reveals that the polarizability is strongly related to the radius of the NP (a^3) but also to the electric properties of the surrounding medium (ε_m). These are two major observations which help to understand the physical properties of AgNPs when further theory is introduced. At this point, the theory shows that charge differences can be generated in AgNPs by

visible light if the particle size is small enough. Equation (21) shows also that the charge polarization is stronger in larger NPs.

References

1. S. Maier. *Plasmonics : Fundamentals and Applications.* Springer, 2007.

2. J. D. Jackson. *Classical electrodynamics.* Wiley, 1999.

3. L. Ohannesian and A. J. Streeter. *Handbook of pharmaceutical analysis.* Marcel Dekker, 2002.

4. J. Lalevee and J. P. Fouassier. *Dyes and Chomophores in Polymer Science.* Wiley, 2015.

Enhancing fluorescence of monomeric bacteriophytochromes by plasmonic nanoparticles

Lauri Nuuttila,[†] Kosti Tapio,[†] Tibebe Lemma,[†] Janne A. Ihalainen,[‡] Nikolai V. Tkachenko,[¶] Jussi Toppari,[*,†] and Heli Lehtivuori[*,†,§]

[†]*University of Jyvaskyla, Nanoscience Center, Department of Physics, P.O. Box 35, University of Jyväskylä, Finland*

[‡]*University of Jyvaskyla, Nanoscience Center, Department of Biological and Environmental Sciences, P.O. Box 35, University of Jyväskylä, Finland*

[¶]*Tampere University of Technology, Laboratory of Chemistry and Bioengineering, P.O. Box 527, Tampere, Finland*

[§]*VU University Amsterdam, Department of Physics and Astronomy, Faculty of Sciences, De Boelelaan 1081, 1081HV, The Netherlands*

E-mail: j.jussi.toppari@jyu.fi; heli.lehtivuori@jyu.fi

Abstract

Deep optical imaging in mammalian tissues requires near infrared fluorescent probes. As an optically active proteins in this particular region, phytochromes have been harnessed as *in vivo* fluorophores. Many studies have been conducted to increase their inherently low fluorescence, although high quantum yield has remained an elusive goal. High field enhancement of surface plasmons provides an alternative platform for external manipulation of spectroscopic properties. Here, we utilize this method and focus on the photophysical and photochemical properties of bacteriophytochromes attached to plasmonic silver nanoparticles. This is the first time such complexes are synthesized or characterized. Measurements showed an enhancement in fluorescence quantum yield and especially in brightness via increased absorption. Most importantly, the coupling to surface plasmons changed the excited state decay profile without affecting considerably the shape of the absorption and emission spectra of the biliverdin chromophore. We prospect that the further development of these bacteriophytochrome-functionalized silver nanoparticles will lead to an exciting breakthrough in biological near infrared fuorescence probes as well as in the understanding of biological processes in phytochromes.

Introduction

Fluorophores in the near infrared (NIR), approximately 650–900 nm, attract constant attention because of their diverse applications in bioimaging, materials science and related fields.[1–3] They allow imaging with minimal autofluorescence and absorption of biomolecules in tissue, as well as low light scattering.[4] The promises of genetically encoded NIR fluorescent proteins have led to a renaissance of engineered fluorescent proteins based on Green Fluorescent Protein (GFP) and its derivatives.[5,6] However, GFP-like proteins are not optimal for deep-tissue imaging, because their emission spectra do not extend to NIR region.

The NIR fluorescence properties of phytochromes have been known for a long time,[7,8]

and especially bacteriophytochromes are promising design templates for NIR fluorescent proteins.[9] The photoactivity of bacteriophytochromes is based on a linear tetrapyrrole Biliverdin IXa (BV) which binds into the protein structure and allows absorption of light in the red and far-red regions of the spectrum.[6,9–12] During the last decade, great effort has gone into improving the photophysical and photochemical properties of microbial phytochrome-based dyes from *Deinococcus radiodurans*,[9–11,13,14] *Rhodopseudomonas palustris*[3,6,12,15–17] and from cyanobacteria.[7,18] Fluorescent phytochromes are an explosively increasing area of current bioimaging research and will have an enormous impact on biological imaging strategies.[19]

Because full-length phytochromes are required for biological activity,[20] the fluorescence protein development is concentrated only on PAS (Per/Arndt/Sim) and GAF (GMP phosphodiesterase/adenyl cyclase/FhlA) domains, which together form a chromophore-binding domain (CBD). In bacteriophytochromes, BV is commonly covalently bind to PAS domain although GAF domain covers it. Wild-type phytochromes are dimers, but residues in the GAF dimer interface have been rationally mutated to create a monomer.[10,13,14]

The initial monomeric CBD from *Deinococcus radiodurans* (CBDmon) has a low fluorescence quantum yield (QY) of $(2.9 \pm 0.1)\%$.[13] In order to improve this, one can engineer the protein so that the kinetics of the competing processes, that take place after excitation, are slowed down. In particular, non-radiative relaxation, in which the isomerization around C15=C16 double bond leading to the first relatively stable photoproduct (Lumi-R), should be minimized.[11,21] For example, the fluorescent properties of cyanobacteriochromes (CBCRs) and cyanobacterial phytochrome Cph1 have been improved by site-selective mutations to achieve the QY of 50% and 70%, respectively.[22] Furthermore, *Rhodopseudomonas palustris* variants that have additional Cys residues binding BV in GAF domain like in plant and cyanobacterial phytochrome, have the QYs of 15%.[17,23] However, the challenge in this kind of development is that usually the high fluorescent QY is located in the orange part of the spectrum ($\sim$ 690 nm). Yet, in *Deinococcus radiodurans*, the fluorescence QY of CBDmon has been improved even to 0.1 by site-selective mutations while still maintaining the

emission around 720 nm.[11,13]

Metal nanoparticles (NP) are known to affect the fluorescence of chromophores, either by enhancing or quenching it.[24,25] These both effects are due to localized surface plasmons (LSP), i.e., the coupled excitations of the electromagnetic field and mechanical oscillations of free electrons in a metal NP.[26,27] If the localized surface plasmon resonance (LSPR) of the NP matches with the emission spectrum of the molecule, the coupling of the molecule to LSP is far more efficient than to a free space photon, due to the higher density of states of the LSP.[25,27] After the LSP excitation in the NP, it radiates very fast leading to total enhancement of the molecular emission and thus QY, or alternatively irradiatively decays via internal dissipation channels of the metal, thus leading to a quenching of the emission. The balance between these two processes depends strongly on type of metal as well as the distance between NP and the molecule.[25,27] Similarly, an increased absorption obtained via matching the LSPR to the molecular absorption spectrum, leads to enhanced total fluorescence and brightness.

In this paper, we introduce a way to improve fluorescence properties of bacteriophytochromes by using plasmonic spherical silver nanoparticles (AgNPs). This type of method has formerly been used to increase fluorescence of dyes,[28] quantum dots,[29] and GFP.[30] For this purpose we have developed a chemical synthesis to attach the CBDmon proteins to AgNPs. With these complexes, we show that the fluorescence QY and especially brightness of the bacteriophytochrome are greatly enhanced by surface plasmons so that the maximum fluorescence still remains in the original place. This will open many new possibilities for bioimaging and -sensing applications. In addition, understanding the interactions between biological macromolecules and plasmonic metal NPs is a currently relevant scientific issue due to increased impact of NPs on the biosphere in the near future.[31]

Experimental Section

Protein expression. Unless otherwise indicated, all reagents and solvents were obtained from commercial suppliers and used without further purification. The constructs encoding the monomeric CBD fragment of the DrBphP bacteriophytochrome (amino acids 1-321) are described elsewhere.[10,13] CBDmon was expressed in *Escherichia coli* strain BL21 (DE3) and purified by affinity and size-exclusion chromatography as in Ref.[32] The purified proteins were concentrated to 20 mg/mL in the final buffer Tris-HCl pH 8.0 (30 mM), flash-frozen, and stored at -80°C. Before measurement, the phytochrome samples were quickly thawed and filtered with 0.22 μm centrifugal filters (Amicon Ultrafree, Millipore) and diluted with the final buffer.

AgNP-CBDmon sample preparation. Sample preparation is illustrated in Fig. 1. AgNPs were prepared as in Ref.[33] Briefly, silver nitrate (AgNO$_3$) of a quantity of 34 mg was dissolved in 200 mL of distilled water and brought to boiling. After the mixture started boiling, 4 mL of trisodium citrate (Na$_3$C$_6$H$_5$O$_7$, TSC) solution (1% by weight) was added to the mixture. TSC acts as a reducing and stabilizing agent. After this, the solution was kept on boiling for 1 h while refluxing the evaporating water. Remained 200 mL of grey-yellow AgNP solution was cooled down to room temperature and the smallest AgNPs (< 60 nm) were collected by centrifuging the solution for 1 h with 100$\times$g and discarding the formed pellet.

N,N-Bis(carboxymethyl)-L-lysine hydrate (BCML) coated AgNPs (AgNP-BCML) were prepared by adding 1 mg/mL of BCML into 1.5 mL of AgNPs solution and stirring the solution for 24 h at room temperature. Unreacted BCML was removed by centrifuging the AgNP-BCML solution and replacing the supernatant with water several times. Hereafter the particles were dissolved in 0.5 mL of Tris-HCl, pH 8.0 (30 mM) buffer. The binding ability of BCML to AgNPs was confirmed by agarose gel electrophoresis assay, atomic force microscopy (AFM) and LSPR spectroscopy. For electrophoresis, the freshly prepared AgNP and AgNP-BCML samples were loaded on 0.5% agarose gel, prepared using TBE buffer. The

gel was run at 150 V for 45 min and subsequently imaged using a CoolSNAP HQ2 camera (Roper Scientific). Other validation methods are explained below.

CBDmon coated AgNP-BCML (AgNP-CBDmon) were prepared in dark by mixing 5 μL of 0.83 mM CBDmon and 0.6 mg of Nickel(II)chloride ($NiCl_2$) to the AgNP-BCML solution while stirring. The solution was left stirring for 2 min and finally washed with Tris-HCl, pH 8.0 (30 mM) buffer by centrifuging several times. A protocol for the sample preparation is summarized in Fig. 1, with a schematic diagram of each step shown in the upper panel, while the results of the test confirming each step are collected to the lower panels.

Spectroscopic measurements and data analysis. Unless otherwise stated, all the measurements are carried out at room temperature.The steady-state absorption spectra were recorded using Perkin Elmer LAMBDA 850 UV-Vis absorption spectrophotometer. Obtained spectra were used for determination of CBDmon concentration in the samples. The femtosecond pump-probe technique was used to measure transient absorption spectra with time resolution down to 0.15 ps. Ti:sapphire laser (Libra-F, Coherent Inc.) and optical parametric amplifier (Topas-C, Light Conversion Ltd.) were used to produce pump and probe pulses in the ExciPro (CDP) measurement system as previously described.[34] To avoid excessive degradation, the measurements were conducted in a 0.25 mm flow cell. The sample solution (volume 0.4 mL) was cycled using a peristaltic pump (Masterflex C/L) at a flow rate of 0.2 mL/min through the flow cell, a glass reservoir, and a connecting Teflon tubing with the 0.25 mm inner diameter. A Fiber-Coupled LED (780±15 nm, 3 mW, Thorlabs) was used to keep the sample in the Pr form by constantly illuminating the sample through the Teflon tubing. The OD_{700} of the samples was about 0.45. The 640±10 nm pump pulse with energy density of 0.026 mJ/cm^2 were used to excite the CBD and AgNP-CBDmon samples. The transition absorption were measured in the spectral range 530–770 nm.

The steady-state fluorescence measurements were performed using a Varian Cary Eclipse fluorescence spectrophotometer with excitation wavelengths of 390 nm and 630 nm. The samples were diluted to the OD_{700} less than 0.1 and the fluorescence QYs were determined

relative to the genuine CBDmon.[13] QYs of CBDmon in AgNP-CBDmon complexes were calculated by using the absorption spectra to estimate the concentration of CBDmon in the complex. Brightness of the AgNP-CBDmon samples was calculated as a percentage of CBDmon brightness using formula[35]

$$\frac{B_{\text{F}}}{B_{\text{R}}} = \frac{\varepsilon_{\text{F}}\phi_{\text{F}}}{\varepsilon_{\text{R}}\phi_{\text{R}}} = \frac{A_{\text{F}}c_{\text{R}}\phi_{\text{F}}}{A_{\text{R}}c_{\text{F}}\phi_{\text{R}}}, \tag{1}$$

where B is the brightness, ε the extinction coefficient, ϕ the QY, c the concentration and A the absorption of the sample at the excitation wavelength. Subindex F refers to AgNP-CBDmon complex and R to reference, i.e., genuine CBDmon.

The fluorescence decays were measured using a time-correlated single photon counting (TCSPC) system consisting of a HydraHarp 400 controller and a PDL 800-B driver (PicoQuant GmBH) as previously described.[11] The excitation wavelengths were 375 nm and 660 nm from a pulsed diode laser heads LDH-D-C-375 and LDH-P-C-660, respectively. The repetition rate of the excitation pulses was set to 40 MHz, and the output power of the lasers were 1.2 mW. The fluorescence signal was detected with a single photon avalanche photodiode (SPAD, MPD-1CTC) through a 720±10 nm band-pass filter (Thorlabs). The time resolution was approximately 60–70 ps (full width at half-maximum (FWHM) of the instrument response function (IRF)).

The transient absorption and fluorescence data were analyzed using the global multi-exponential programs Pygspec[36] and Glotaran.[37] The time evolution of the laser-induced absorption difference spectra were analyzed by approximating the data by a sum of exponentials deconvoluted with a Gaussian representing the laser pulse. By using simple, parallel decay model or a sequential decay model, the common lifetimes τ_i for decay associated difference spectra (DADS) and evolution associated difference spectra (EADS) were obtained, respectively.[38] Throughout the manuscript, the EADS are shown in the main text and the corresponding DADS are shown in SI Fig. 9.

Imaging. For transmission electron microscope (TEM), 5 μL of AgNP, AgNP-BCML and AgNP-CBDmon solutions were dropped onto Formvar coated copper grids. Specimens were nitrogen-dried for 4 h and imaged by JEM-1400 (JEOL Corporation) microscope with an acceleration voltage of 80 kV.

For atomic force microscope (AFM), glass plates were immersed in HCl/HNO$_3$ (3:1) for 30 min and thereafter rinsed with distilled water. Cleaned glass plates were air-dried and immersed in 2% ethanol solution of 3-aminopropyltriethoxysilane (APTES) for 3 min, followed by 5 min sonication with pure ethanol and water. Finally, the APTES films were heated on a hot plate for 1 h at 90°C. Few droplets of AgNPs and AgNP-BCML solution, prepared from the commercial 20 nm AgNP solution (Sigma-Aldrich), were deposited onto APTES films and incubated for 1 h followed by rinsing with deionized water. Prepared glass plates were sonicated for 5 min in water and the attached AgNPs and AgNP-BCMLs were imaged in air with Dimension Icon AFM (Bruker) in tapping mode with 0.5-1.0 Hz scan rate.

Results and Discussion

Sample characterisation. The synthesis protocol and schematic representations of reactions involved in attaching CBDmons to AgNPs are shown in the upper part of Fig. 1. First, a ligand exchange of BCML was performed on the citrate coated AgNPs as in Doo *et al.*[39] Then, Nickel ions (Ni^{2+}) were used to form a 1:1 complex with carboxylate (RCOO$^-$) of the BCML[40,41] followed by addition of CBDmon, which forms two strong hydrogen bonds between the histidine tag of the protein and Ni^{2+}, thus, forming the final AgNP-CBDmon complex. The formation of AgNPs, AgNP-BCML, and finally AgNP-CBDmon complex were confirmed at different reaction steps by using a UV-Vis absorption spectra, gel electrophoresis, as well as AFM and TEM imaging. Results from these measurements are shown in the lower part of the Fig. 1 with single background color corresponding to each step (red, green,

blue).

The characteristic absorption maximum, that is, the LSPR band maximum of AgNPs, freshly fabricated along the method described above, is at 417±4 nm (see Fig. 1). The concentration and size of the particles in the solutions were estimated to be 3±2 pM and 46±5 nm, respectively, according to Paramelle *et al.*[42] In addition, the TEM images showed roughly spherical AgNPs with diameter of 40–50 nm, which agrees nicely with our spectroscopic data. The LSPR band of the ready AgNP-BCML complex has approximately the same bandwidth and peak position with only tiny redshift of 0–3 nm (see Fig. 1). This indicates that the LSPR of the NPs are not affected by the ligand exchange, and the redshift is likely due to the change of the refractive index in the vicinity of the particle implying successful attachment.[43,44]

The BCML ligands increase the amount of charges on the surface compared to the citrate coated AgNPs which helps to separate individual AgNPs from each other. Thus, the formation of AgNP-BCML can be further confirmed by increased mobility of NPs in the agarose gel electrophoresis as clearly seen in the lower right corner of Fig. 1. The separation of the individual AgNPs can be seen also in TEM images as an appearance of gaps between the NPs. This type of behavior was not seen with citrate coated AgNPs sample (see Fig. 1). In addition, BCML attachment to commercial AgNPs was confirmed by using AFM (SI Figs. 5&6). Commercial AgNPs were used here, because they have a homogeneous size distribution (SI Fig. 7). Diameters were determined from the height profiles of randomly selected NPs and the results were fitted by Gaussian distribution, yielding unimodal size distribution of 17±4 nm for AgNPs and 20±4 nm for AgNP-BCML. The difference of the size distribution is approximately 3 nm, which is near the size of BCML calculated from the chemical structure (2.4 nm) (SI Figs. 8). Lower left corner of Fig. 1 shows AFM images of typical AgNPs and AgNP-BCMLs together with their height profiles, as well as the histograms of the determined diameters.
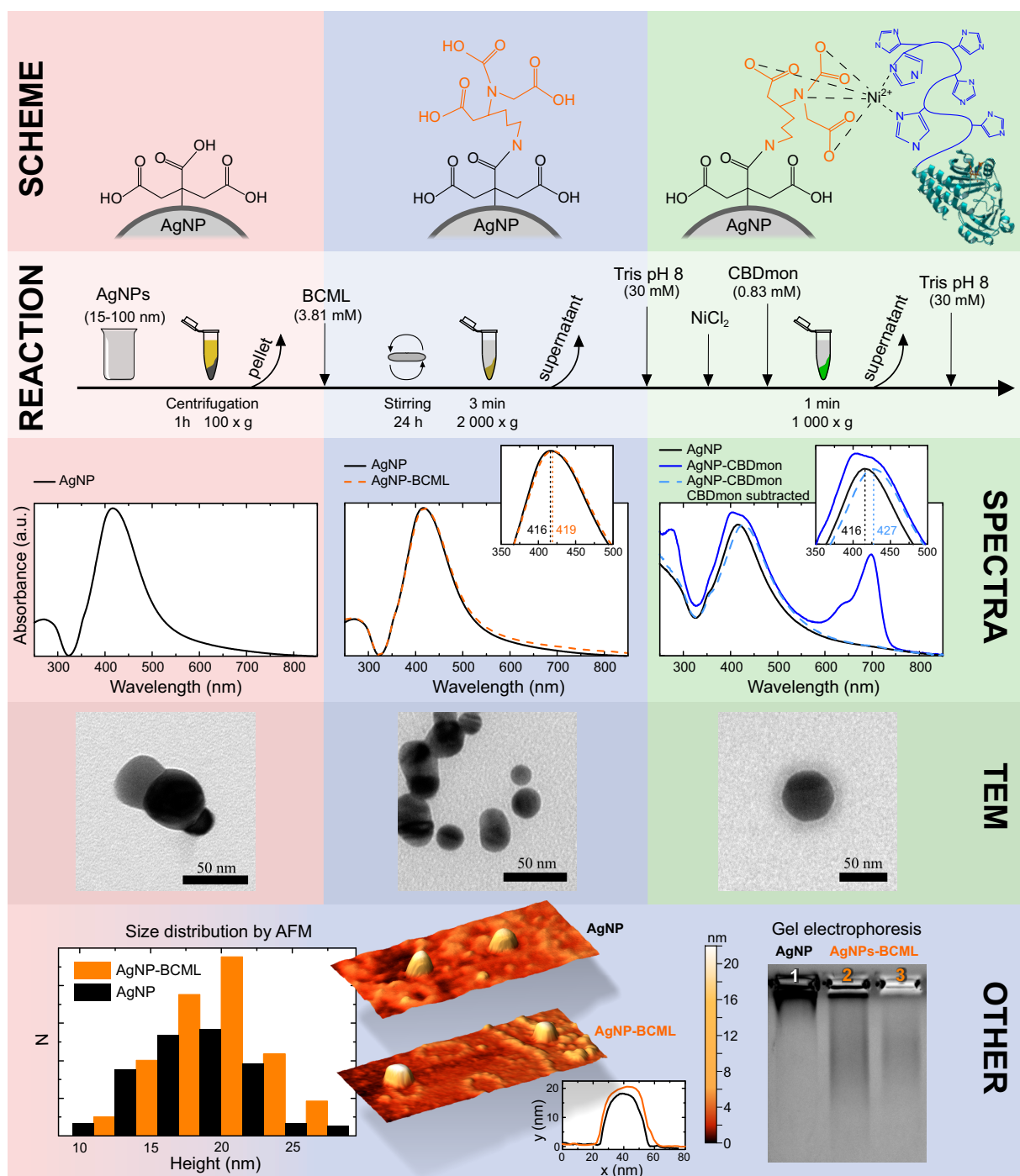
Figure 1: The synthesis protocol for fabrication of AgNP-CBDmon complex (REACTION) with a schematic illustration of each step (SCHEME). Synthesis was thoroughly followed by UV-Vis absorption (SPECTRA), in particular via a redshift of the AgNP LSPR, and a thin veil appearing around the particles in AgNP-CBDmon TEM images (TEM). In addition, increased diameter in AFM and better mobility in agarose gel electrophoresis were used to confirm the BCML attachment to AgNPs (OTHER). The colors indicate each step of the synthesis including the corresponding scheme and results of the confirming experiments. For more detailed discussion see text.

Attachment of CBDmon to AgNP-BCML can also be verified by multiple methods. The absorption spectra of AgNP-CBDmon samples have peaks which belong to CBDmon, a Soret band at 390 nm and Q-band at 698 nm (Fig. 1).[10,13,45] In some AgNP-CBDmon samples, the Q-band of CBDmon becomes broader after the attachment to AgNPs (SI Fig. 2), which can be attributed to aggregation of the CBDmon molecules, like the other tetrapyrrole molecules.[46,47] Most likely CBDmon forms irregular aggregates on top of the AgNPs, as a result of their flexible linkers and the accompanying Ni^{2+} ions. The subtraction of the CBDmon absorption from the spectrum of AgNP-CBDmon gives the LSPR band of AgNPs in the AgNP-CBDmon sample (Fig. 1). The LSPR spectrum has almost the same shape and bandwidth as before the attachment of the CBDmon, indicating that again the core size of the particles is not affected by the ligand exchange. However, the LSPR band maximum is redshifted by 11 ± 1 nm from the original citrated coated AgNPs band. The redshift is again due to the change of the refraction index which is larger in the case of phytochrome than in the BCML ligand addition. In addition, a clear thin veil appears around AgNPs in the TEM images of AgNP-CBDmon sample. The size of this veil in TEM images is approximately 8 nm which is around the diameter of CBDmon.[10]

Fluorescence properties. We collected the fluorescence spectra of CBDmon and AgNP-CBDmon (SI Figs. 3&4), when excited at the Soret and Q-bands of BV, i.e., at 390 nm and 630 nm, respectively, from altogether eleven samples (listed in Table 1). Typical spectra, recorded from sample 10, are presented in Fig. 2A. The observed fluorescence, originating from the BV chromophore, has the same spectral shape and peak position ($\sim$720 nm) in both CBDmon and AgNP-CBDmon samples, which is in keeping with their matching absorption spectra (see Fig. 1).

From the fluorescence spectra, we determined the fluorescence QYs, ϕ_{390} and ϕ_{630} for CBDmon in the presense of AgNPs (see Table 1). For the average ϕ_{630} of all the AgNP-CBDmon samples, we obtained $(3.48\pm0.12)\%$, which is 20% higher than the fluorescence QY of genuine CBDmon, i.e. $(2.9\pm0.1)\%$.[13] Similar QY increasement was observed at 390 nm
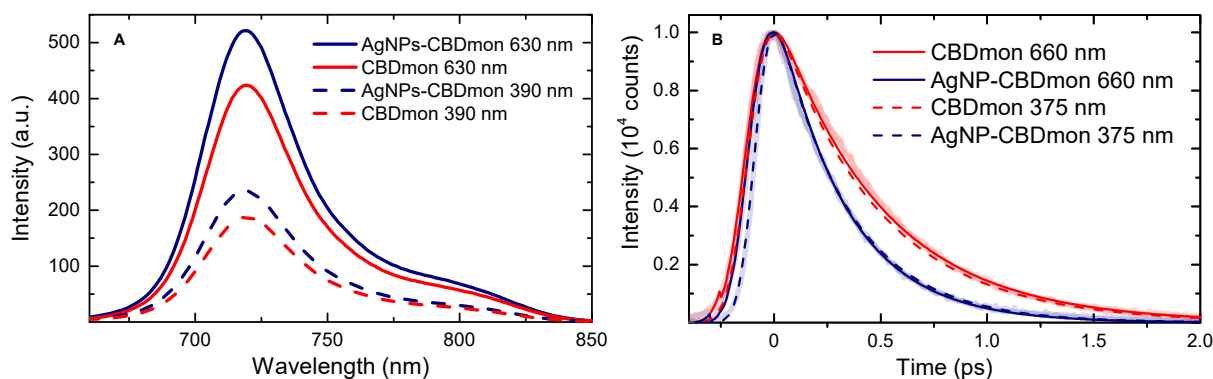
Figure 2: (A) Fluorescence spectra of AgNP-CBDmon (blue) and CBDmon (red) which were excited at 630 nm (solid) or 390 nm (dashed). Spectra were corrected by the number of absorbed photons. (B) Emission decays of AgNP-CBDmon (blue) and CBDmon (red) excited at 630 nm (solid) or 390 nm (dashed) and monitored at 720 ± 10 nm. All the curves are recorded from the sample **10**, except the decay with 660 nm excitation is from sample **8**.

excitation wavelength. This is a welcome result given the impetus to find a NIR fluorescence protein with a high QY. The fact that the enhancement of the fluorescence QY is only 20% and, particularly, the same for both excitations ($\phi_{390} \approx \phi_{630}$), implies that attachment to AgNPs does not considerably affect the CBDmon reaction pathways.

The brightness values B_{390} and B_{630} for AgNP-CBDmon samples were determined using the QY and extinction coefficient of the whole AgNP-CBDmon complex. Excluding the sample 11, the average B_{390} and B_{630} were $(470 \pm 40)\%$ and $(134 \pm 11)\%$, respectively, which is a significantly higher enhancement than in QY. The improvement of the brightness is not the same for both excitations, but three times higher, when a sample is excited at 390 nm. The result is nicely in line with the fact that the absorption at 390 nm is perfectly overlapping with the LSPR band of the AgNPs and 630 nm not. Because of this, the increase in absorbance is higher around 390 nm producing more enhanced brightness. The sample 11 has both the highest brightness as well as QY enhancement. The better enhancement in QY most probably originates from the AgNP aggregation, which results in a LSPR spectrum covering also the emission wavelength (see SI Fig. 4). Highly increased QY together with increased absorption yields enormous enhancement in brightness. We can thus deduce the AgNP aggregation to be a major causal factor in increased brightness for the AgNP-CBDmon

complex.

It seems, that in optimal conditions and sufficient size (40–50 nm) of the AgNPs, AgNP-CBDmon complex leads to a fluorescence enhancement via increased QY. In addition, there is seen a significant negative correlation of the fluorescence QY with the CBDmon concentration (-0.775; p-value 0.009) but not with the AgNP concentration (0.572; p-value 0.084). This means that most likely CBDmon aggregates on the surface of AgNPs when it has been added in excess. This result agrees nicely with our absorption measurements of AgNP-CBDmon samples, where we observe broadening of the Q-band in some cases, which can also be a sign of AgNP aggregation.

Excited state lifetime measurements provide information about fluorescence properties independent of the concentration of the sample. The fluorescence decay of BV molecules in the protein binding pocket was studied by a TCSPC method with an excitation wavelengths of 375 and 660 nm and monitoring wavelength of 720 nm. Typical decay curves for both AgNP-CBDmon and CBDmon samples are presented in Fig. 2B. The fluorescence decays were fitted with either mono- or biexponential functions[32] to obtain the excited state lifetimes, τ_{375} and τ_{660} of AgNP-CBDmon and CBDmon. We found, that the decay profile of the CBDmon required two exponential components,[13] whereas in the case of AgNP-CBDmon, monoexponential fits were sufficient (see Table 1). By comparing the average τ_{660} of the AgNP-CBDmon samples and CBDmon, we can conclude that the lifetime is about 30% shorter in the case of AgNP-CBDmon. A similar decrease in decay time was observed with 375 nm excitation wavelength. This indicates that CBDmon molecules are indeed attached to the AgNPs and their relaxation time is shortened due to metal-enhanced fluorescence (and/or quenching).

The excited-state absorption. Time-resolved absorption spectroscopy (pump–probe) in a picosecond time scale was used to monitor the relaxation processes of the photoexcited CBDmon and AgNP-CBDmon. Nearly selective excitation of CBDmon is possible because of the different absorption maxima of CBDmon Q-band and AgNPs (Fig. 1). Pump–probe

Table 1: Properties of the prepared samples with measured QYs and calculated decay fits for TCSPC and pump-probe.[+]

#	c_{CBD} (nM)	$\underline{c_{CBD}}$ c_{Ag} $\cdot 10^4$	ϕ_{390} (%)	ϕ_{630} (%)	B_{390} (%)	B_{630} (%)	TCSPC τ_{375} (ps)	τ_{660} (ps)	pump-probe τ_1 (ps)	τ_2 (ps)	τ_3 (ns)
0	2390	-	0,76	2.9*	100	100	380&580[A]	390&620[B]	5	380	> 6
1	550	11.4	0.84	3.8	365	174	-	-			
2	660	15.5	0.78	3.2	374	125	-	-			
3	380	8.6	1.3	5.2	649	200	-	-			
4	810	20.9	0.88	3.2	589	149	-	-			
5	1790	40.3	0.69	2.8	460	132	-	-			
6	2150	70.5	0.82	3.0	546	140	-	-			
7	1800	77.7	0.80	2.9	530	135	-	-			
8	1490	105	0.66	2,2	338	78	-	316			
9	2620	238	0.53	1.9	296	73	-	-			
10	1130	406	0.94	3.6	516	129	330	346			
11	820	85.3	-	6.3	-	5017	-	-	0.3	130	-

[+] c_{CBD} and c_{Ag} are concentrations of CBDmon and AgNPs in the prepared sample. ϕ is measured QY of CBDmon in the presence of AgNPs at 390 nm or 630 nm and B is the calculated brightness of AgNP-CBDmon in respect to the pure CBDmon. τ_{375} and τ_{660} are single exponential lifetimes for TCSPC and τ_1, τ_2 and τ_3 lifetimes for pump-probe.
* determined from literature.[13]
[A,B] percentual contributions to the lifetime are 72% and 28% for A or 67% and 33% for B.[13]

measurements for the CBDmon and AgNP-CBDmon were done by exciting only the BV at 640 nm. The resulting transient absorption (TA) spectra are shown in Fig. 3. AgNP absorption at this wavelength is minor and no transient signal of AgNPs and AgNP-BCML samples were seen with this excitation (data not shown).

The TA spectra of CBDmon show features that were previously reported for other bacteriophytochromes[21,48,49] and cyanobacterial phytochromes[50,51] in the 670–800 nm region. The short-lived EADS can be attributed to ground state bleaching of the Q-band together with stimulated emission and excited state absorption. At longer time delay an induced absorption at 730 nm appears (Fig. 3B), which can be assigned to the formation of Lumi-R state.[21,48,49] The time course of the difference spectra were analyzed using multiexponential global fitting with a sufficient number of exponential components. Three components were
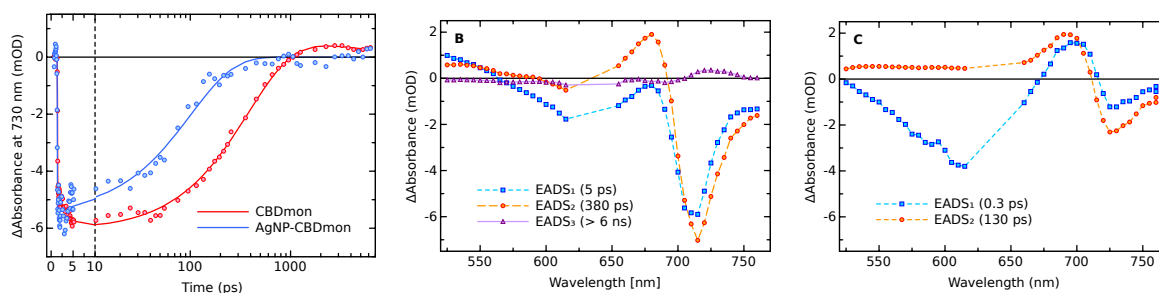
Figure 3: (A) Transient absorption decays of CBDmon (red) and AgNP-CBDmon samples (blue) at 730 nm. Evolution-associated difference spectra (EADS) of (B) CBDmon and (C) AgNP-CBDmon samples. CBDmon and AgNP-CBDmon samples were excited at 640 nm and TA data are recorded from the samples 0 and 11.

required for to obtain a reasonable fit of CBDmon data, which gave lifetimes of $\tau_1 = 5$ ps, $\tau_2 = 380$ ps, and $\tau_3 > 6$ ns. The resulting EADS are depicted in Fig. 3B and the decay-associated difference spectra (DADS) in SI Fig. 9A. These three EADS lifetimes are typically observed also in other bacteriophytochromes.[21,48,49] The first EADS with the lifetime of 5 ps corresponds to the initial excited state processes of the chromophore.[21] The second EADS corresponds to the excited state decay with the lifetime of 380 ps. This interpretation is consistent with the time-resolved fluorescence measurements (Fig. 2B) which indicate the first exponential decay with a similar 390 ps time constant.[13] The third EADS corresponds to a decay of the Lumi-R state with the lifetime longer than 6 ns thus exceeding the detection time window.

The amplitude of the Lumi-R is very low with a remaining bleach of about 8% of the initial signal amplitude. Accounting for the fluorescence QY of 2.9%, this observation indicates that the vast majority (about 90%) of the BV excited states relax nonradiatively to the Pr ground state. In addition, our study shows that fluorescence QY and the QY of the Lumi-R formation increases slightly in the CBDmon sample relative to the dimer CBD.[10,13] This change in a photochemical property implies that the monomerization affects the surroundings of BV even though no amino acids have been changed near the chromophore.[13] These small changes might be due to larger flexibility of the protein, better solvent access, or another factors.[10,13]

Typical transient absorption curves at 730 nm with their fits are shown for both CBDmon (sample 0) and AgNP-CBDmon (sample 11) in Fig. 3A. By comparing these two traces one can clearly see that the decay is three times faster when AgNPs are present. This result is similar to our time-resolved fluorescence measurements. Surprisingly, only a biexponential function was needed to fit the transient absorption spectra of AgNP-CBDmon sample (Fig. 3C). The first EADS with the lifetime of 0.3 ps, has a very different shape and is about twice as intense around 620 nm compare to the spectrum of CBDmon sample measured under identical excitation conditions (Fig. 3B). Moreover, its shape cannot be obtained as a combination of TA spectra of the bare AgNPs and CBDmon samples. Thus, this negative band most probably belongs to the aggregated silver nanoparticles, which induce a red tail to the LSPR spectrum, as recorded for the sample 3 (SI Fig. 10). However, a positive band at 700 nm and a negative signal at 720 nm corresponds to the CBDmon moiety. Yet, in comparison with the TA spectrum of the CBDmon sample, these bands are redshifted by approximately 10 nm. The obtained lifetime of 0.3 ps is also much shorter than that of CBDmon, as expected.

The second EADS with the lifetime of 130 ps corresponds to excited state decay and its shape is quite similar to the second EADS of CBDmon sample. All peaks are redshifted by roughly 10 nm compered to the bare CBDmon sample. In addition, the negative signal at 730 nm, which corresponds to the excited state decay of CBDmon, is three times smaller. These all features show that, the excited state kinetics of CBDmon are strongly influenced by the AgNPs. In addition, CBDmon have induced absorption at 730 nm, which is absent in AgNP-CBDmon sample. The reason for this is unclear and it should be studied separately. Nevertheless, the absence of the slowest EADS implies that there is no Lumi-R formation in CBDmon attached to AgNP, which is a desired result and also contributes to the overall fluorescence enhancement.

Conclusions

Bacteriophytochrome-functionalized 40–50 nm silver nanoparticles (AgNP-CBDmon) can be easily prepared by a ligand exchange of BCML on the citrate coated AgNPs and by using His-tag to connect CBDmon and AgNPs. Attachment of BCML to AgNP as well as CBDmon to AgNP-BCML can be confirmed with multiple spectrocopy and microscopy techniques. The absorption spectrum of CBDmon have almost the same shape and bandwidth as before the complex formation, indicating that the bacteriophytochromes are not affected by the AgNPs. However, LSPR band of AgNPs redshifts as the refractive index changes during ligand and CBDmon addition. The phytochromes are tightly packed on the surface of the silver nanoparticles in the AgNP-CBDmon, which is seen in spectroscopy as well as in TEM images. The interactions between CBDmon and AgNPs were observed by steady-state as well as time-resolved absorption and fluorescence spectroscopies. The fluorescence QY and brightness of CBDmon is enhanced by surface plasmons so that the maximum fluorescent still remains in the original place. The overall fluorescence QY of CBDmon is still low, but, the brightness improved significantly. In addition, enhancement is clearly higher for the aggregated AgNP sample (sample 11) most probably due to widened LSPR spectrum overlapping also with emission of the CBDmon. In overall, the plasmonic enhancement of bacteriophytochrome fluorescence is a promising method providing clear fluorescent enhancement without affecting the spectral properties. However, AgNP-CBDmon interaction processes require further studies in order to find out in detail the effect of, e.g., solvent, AgNPs size and shape, length and type of linkers and packing density of the chromophores.

Acknowledgement

References

(1) Escobedo, J. O.; Rusin, O.; Lim, S.; Strongin, R. M. NIR Dyes for Bioimaging Applications. *Curr Opin Chem Biol.* **2010**, *14*, 64–70.

(2) Hilderbrand, S. A.; Weissleder, R. Near-infrared fluorescence: application to in vivo molecular imaging. *Curr Opin Chem Biol.* **2010**, *14*, 71–79.

(3) Shcherbakova, D. M.; Shemetov, A. A.; Kaberniuk, A. A.; Verkhusha, V. V. Natural Photoreceptors as a Source of Fluorescent Proteins, Biosensors, and Optogenetic Tools. *Annu Rev Biochem.* **2015**, *84*, 519–550.

(4) Weissleder, R. A clearer vision for in vivo imaging. *Nat. Biotechn.* **2001**, *19*, 316–316.

(5) Marx, V. Probes: seeing in the near infrared *Nat Methods* **2014**, *11*, 717.

(6) Shcherbakova, D. M.; Baloban, M.; Verkhusha, V. V. Near-infrared fluorescent proteins engineered from bacterial phytochromes. *Curr. Opin. Chem. Biol.* **2015**, *27*, 52–63.

(7) Fischer, A. J.; Lagarias, J. C. Harnessing phytochrome's glowing potential. *Proc. Natl. Acad. Sci. USA* **2004**, *101*, 17334–17339.

(8) Wagner, J. R.; Zhang, J.; von Stetten, D.; Günther, M.; Murgida, D. H.; Mroginski, M. A.; Walker, J. M.; Forest, K. T.; Hildebrandt, P.; Vierstra, R. D. Mutational Analysis of Deinococcus radiodurans Bacteriophytochrome Reveals Key Amino Acids Necessary for the Photochromicity and Proton Exchange Cycle of Phytochromes *J. Biol. Chem.* **2008**, *40*, 12212–12226.

(9) Shu, X.; Royant, A.; Lin, M. Z.; Aguilera, T. A.; Lev-Ram, V.; Steinbach, P. A.;
Tsien, R. Y. Mammalian Expression of Infrared Fluorescent Proteins Engineered from
a Bacterial Phytochrome. *Science* **2009**, *324*, 804–807.

(10) Auldridge, M. E.; Satyshur, K. A.; Anstrom, D. M.; Forest, K. T. Structure-guided En-
gineering Enhances a Phytochrome-based Infrared Fluorescent Protein. *J. Biol. Chem.*
2012, *287*, 7000–7009.

(11) Lehtivuori, H.; Bhattacharya, S.; Angenent-Mari, N. M.; Satyshur, K. A.; Forest,
K. T. Removal of Chromophore-Proximal Polar Atoms Decreases Water Content and
Increases Fluorescence in a Near Infrared Phytofluor. *Front Mol Biosci.* **2015**, *2*, 65.

(12) Shcherbakova, D. M.; Baloban, M.; Emelyanoc, A. V.; Brenowitz, M.; Guo, P.;
Verkhusha, V. V. Bright monomeruc near-infrared fluorescent proteins as tags and
biosensors for multiscale imaging. *Nat Commun.* **2016**, *7*, 12405–63.

(13) Bhattacharya, S.; Auldridge, M. E.; Lehtivuori, H.; Ihalainen, J. A.; Forest, K. T.
Origins of Fluorescence in Evolved Bacteriophytochromes. *J. Biol. Chem.* **2014**, *289*,
32144–32152.

(14) Yu, R.; Gustafson, W. C., Han, C.; Lafaye, C.; Noirclerc-Savoye, M.; Ge, W.-P.; Thayer,
D. A.; Huang, H.; Kornberg, T. B., Royant, A.; Jan, L. Y.; Jan, Y. N.; Weiss, W. A.
Shu, X. An improved monomeric infrared fluorescent protein for neuronal and tumour
brain imaging. *Nat. Comm.* **2008**, *5*.

(15) Filonov, G. S.; Piatkevich, K. D.; Ting, L. M.; Zhang, J.; Kim, K.; Verkhusha, V. V.
Bright and stable near-infrared fluorescent protein for in vivo imaging. *Nat. Biotechnol.*
2011, *29*, 757–761.

(16) Piatkevich, K. D.; Subach, F. V.; Verkhusha, V. V. Far-red light photoactivatable near-
infrared fluorescent proteins engineered from a bacterial phytochrome. *Nat. Commun.*
2013, *4*.

(17) Hontani, Y.; Shcherbakova, D. M.; Baloban, M.; Zhu, J.; Verkhusha, V. V.; Kennis, J. T. M. Bright blue-shifted fluorescent proteins with Cys in the GAF domain engineered from bacterial phytochromes: fluorescence mechanisms and excited-state dynamics. *Sci. Rep.* **2016**, *6*, 37362.

(18) Rodriguez, E. A.; Tran, G. N.; Crisp, J. L.; Shu, X.; Lin, J. Y.; Tsien, R. Y. A far-red fluorescent protein evolved from a cyanobacterial phycobiliprotein. *Nat. Meth.* **2016**, *13*, 763–769.

(19) Baloban, M.; Shcherbakova, D. M.; Pletnev, S.; Pletnev, V. Z.; Lagarias, J. C.; Verkhusha, V. Designing brighter near-infrared fluorescent proteins: insights from structural and biochemical studies. *Chem. Sci.* **2017**, *8*, 4546–4557

(20) Yang, X,; Kuk, J.; Moffat, K. Crystal structure of Pseudomonas aeruginosa bacteriophytochrome: Photoconversion and signal transduction. *Nat. Comm.* **2014**, *105*, 14715–14720.

(21) Toh, K. C.; Stojković, E. A.; van Stokkum, I. H.; Moffat, K.; Kennis, J. T. Fluorescence quantum yield and photochemistry of bacteriophytochrome constructs. *Phys. Chem. Chem. Phys.* **2011**, *13*, 11985–11997.

(22) Sun, Y. F.; Xu, J. G.; Tang, K.; Miao, D.; Gärtner, W; Scheer, H.; Zhao, K. H.; Zhou, M. Orange fluorescent proteins constructed from cyanobacteriochromes chromophorylated with phycoerythrobilin. *Photochem. Photobiol. Sci.* **2014**, *13*, 757–763.

(23) Stepanenko, O. V.; Baloban, M.; Bublikov, G. S.; Shcherbakova, D. M.; Stepanenko, O. V.; Turoverov, K. K.; Kuznetsova, I. M.; Verkhusha, V. V. Allosteric effects of chromophore interaction with dimeric nearinfrared fluorescent proteins engineered from bacterial phytochromes. *Sci. rep.* **2016**, *6*, 18750.

(24) Morawitz, H.; Philpott, M. R. Coupling of an excited molecule to surface plasmons *Phys. Rev. B* **1974**, *10*, 4863–4868.

(25) Barnes, W. L. Fluorescence near interfaces: the role of photonic mode density. *J. Mod. Opt.* **1998**, *45*, 661–699.

(26) Maier, S. A. *Plasmonics: Fundamentals and Applications*, Springer: New York, 2006.

(27) Chen, H.; Schatz, G. C.; Ratner, M. A. Experimental and theoretical studies of plasmon–molecule interactions. *Rep. Prog. Phys.* **2012**, *75*, 096402.

(28) Zhang, J.; Fu, Y.; Chowdhury, M. H.; Lakowicz, J. R. Metal-enhanced single-molecule fluorescence on silver particle monomer and dimer: coupling effect between metal particles. *Nano Lett.* **2007**, *7*, 2101–2107.

(29) Li, Y.-Q.; Guan, L.-Y.; H-L. Zhang, H.-L.; Chen, J.; Lin, S.; Ma, Z.-Y.; Zhao, Y.-D. Distance-Dependent Metal-Enhanced Quantum Dots Fluorescence Analysis in Solution by Capillary Electrophoresis and Its Application to DNA Detection. *Anal. Chem.* **2011**, *83*, 4103–4109.

(30) Fu, Y; Zhang, J; Lakowicz, J. R. Metal-enhanced fluorescence of single green fluorescent protein (GFP). *Biochem. Biophys. Research Commun.* **2008**, *376*, 712–717.

(31) Nel, A. E.; Mädler, L.; Velegol, D.; Xia, T.; Hoek, E. M. V.; Somasundaran, P.; Klaessig, F.; Castranova, V.; Thompson, M. Understanding biophysicochemical interactions at the nanobio interface *Nat. Mat.* **2009**, *8*, 543–557.

(32) Lehtivuori, H.; Rissanen, I; Takala, H.; Bamford, J.; Tkachenko, N. V.; Ihalainen J. A. Fluorescence properties of the chromophore-binding domain of bacteriophytochrome from Deinococcus radiodurans. *J. Phys. Chem. B* **2013**, *117*, 11049–11057.

(33) Lee, P. C.; Meisel, D. Adsorption and Surface-Enhanced Raman of Dyes on Silver and Gold Sols. *J. Phys. Chem.* **1982**, *86*, 3391–3395.

(34) Sirbu, D.; Turta, C.; Benniston, A. C.; Abou-Chahine, F.; Lemmetyinen, H.; Tkachenko, N. V.; Wood, C.; Gibson, E. Synthesis and properties of a meso- tris–

ferrocene appended zinc(II) porphyrin and a critical evaluation of its dye sensitised solar cell (DSSC) performance. *RSC Advances* **2014**, *13*, 22733–22742.

(35) Würth, C.; Grabolle, M.; Pauli, J.; Spieles, M.; Resch-Genger, U. Relative and Absolute Determination of Fluorescence Quantum Yields of Transparent Samples. *Nature protocols* bf 2013 *8*.

(36) Tkachenko, N. V.; Rantala, L.; Tauber, A. Y.; Helaja, J.; Hynninen, P. H.; Lemmetyinen, H. Photoinduced electron transfer in phytochlorin-[60]fullerene dyads. *J. Am. Chem. Soc* **1999**, *121*, 9378–9387.

(37) Snellenburg, J. J.; Laptenok, S. P.; Seger, R; Mullen, K. M.; van Stokkum I. H. M. Glotaran: A Java-Based Graphical User Interface for the R Package TIMP. *J. Stat. Softw.* **2012**, *49*, 1–22.

(38) Holzwarth, A. R. Data analysis of time-resolved measurements. Biophysical techniques in photosynthesis *Springer, Netherlands* **1996**, *14*, 75–92.

(39) Doo, R. B.; Won, S. H.; Jung, M. L.; Sunwoo, K.; Jin, Y.;L.; Dongmin, K.; Jong. H. J. Lysine-functionalized silver nanoparticles for visual detection and separation of histidine and histidine-tagged proteins. *Langmuir* **2010**, *26*, 2181–2185.

(40) Graff, R. A.; Swanson, T. M.; Strano, M. Synthesis of Nickel–Nitrilotriacetic Acid Coupled Single-Walled Carbon Nanotubes for Directed Self-Assembly with Polyhistidine-Tagged Proteins *Chem. Mater.* **2008**, *20*, 1824–1829.

(41) Gu, H.; Xu, K.; Xu, B. Biofunctional magnetic nanoparticles for protein separation and pathogen detection. *Chem. Commun.* **2006**, 941–949.

(42) Paramelle, D.; Sadovoy, A.; Gorelik, A.; Free, P.; Hobley, J.; Fernig, D. G. A rapid method to estimate the concentration of citrate capped silver nanoparticles from UV-visible light spectra. *The Analyst* **2014**, *139*, 4855–4861.

(43) Anker, J. N.; Hall, W. P.; Lyandres, O.; Shah, N. C.; Zhao, J.; Van Duyne, R. P. Biosensing with plasmonic nanosensors. *Nat. Mat.* **2008**, *7*, 442–453

(44) Willets, K. A.; Van Duyne, R. P. Localized Surface Plasmon Resonance Spectroscopy and Sensing. *Annu. Rev. Phys. Chem.* **2007**, *58*, 267–297.

(45) Takala, H.; Björling, A.; Linna, M.; Westenhoff, S.; Ihalainen, J. A. Light-induced Changes in the Dimerization Interface of Bacteriophytochromes. *J. Biol. Chem.* **2015**, *290*, 16383–16392.

(46) Chen, K.; Preuss, A.; Hackbarth, S.; Wacker, M.; Langer, K.; Rder, B. Novel photosensitizer-protein nanoparticles for photodynamic therapy: photophysical characterization and in vitro investigations. *J. Photochem. Photobiol. B: Biology* **2009**, *75*, 66–74.

(47) Tom, R. T.; Pradeep, T. Interaction of azide ion with hemin and cytochrome c immobilized on Au and Ag nanoparticles. *Langmuir* **2005**, *21*, 11896–11902.

(48) Mathes, T.; Ravensbergent, J.; Kloz, M.; Gleichmann, T.; Gallagher, K. D.; Woitowich, N. C.; St. Peter, R.; Kovaleva, S. E.; Stojković, E. A.; Kennis, J. T. M. Femto- to Microsecond Photodynarnics of an Unusual Bacteriophytochrome. *J. Phys. Chem. Lett.* **2015**, *6*, 239–243.

(49) Toh, K. C.; Stojković, E. A.; van Stokkum, I. H.; Moffat, K.; Kennis, J. T. Proton-transfer and hydrogen-bond interactions determine fluorescence quantum yield and photochemical efficiency of bacteriophytochrome. *Proc. Natl. Acad. Sci. USA* **2010**, *107*, 9170–9175.

(50) Kim, P. W.; Rockwell, N. C.; Martin, S. S.; Lagarias, J. C.; Larsen, D. S. Heterogeneous photodynamics of the Pfr state in the cyanobacterial phytochrome Cph1. *Biochemistry* **2014**, *53*, 4601–4611.

(51) Kim, P. W.; Rockwell, N. C.; Martin, S. S.; Lagarias, J. C.; Larsen, D. S. Dynamic inhomogeneity in the photodynamics of cyanobacterial phytochrome Cph1. *Biochemistry* **2014**, *53*, 2818–2826.

Supporting Information - Enhancing fluorescence of monomeric bacteriophytochromes by plasmonic nanoparticles

Lauri Nuuttila,[†] Kosti Tapio,[†] Tibebe Lemma,[†] Janne A. Ihalainen,[‡] Nikolai V. Tkachenko,[¶] Jussi Toppari,[*,†] and Heli Lehtivuori[*,†]

[†]*University of Jyvaskyla, Nanoscience Center, Department of Physics, P.O. Box 35, University of Jyväskylä, Finland*

[‡]*University of Jyvaskyla, Nanoscience Center, Department of Biological and Environmental Sciences, P.O. Box 35, University of Jyväskylä, Finland*

[¶]*Tampere University of Technology, Department of Chemistry and Bioengineering, Tampere, Finland*

E-mail: j.jussi.toppari@jyu.fi; heli.lehtivuori@jyu.fi
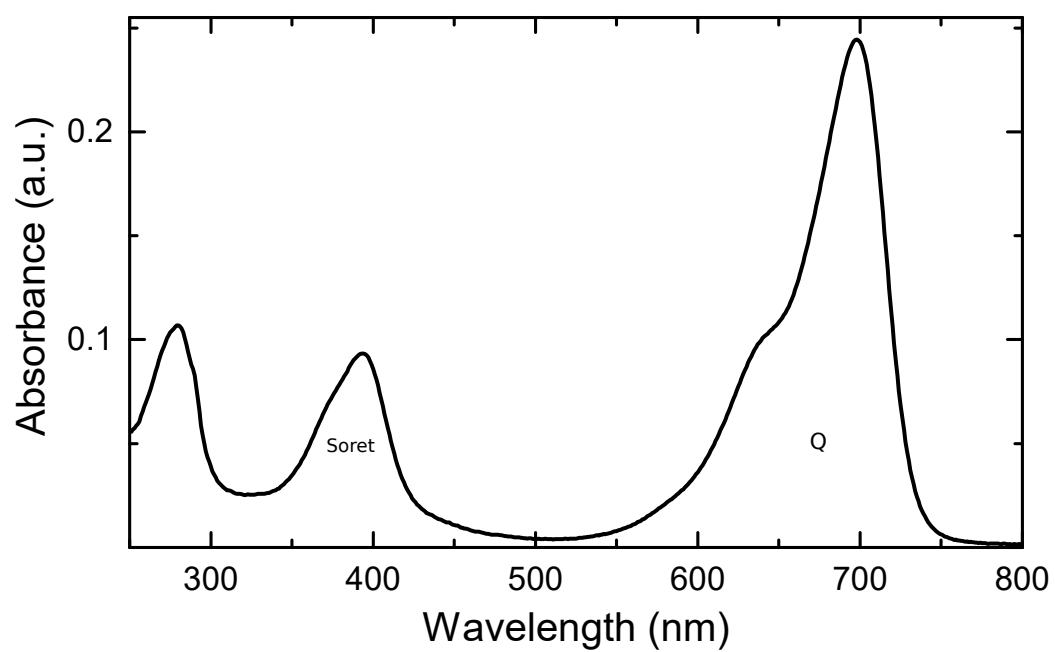
Figure 1: Absorbance of monomeric CBD in pH 8 Tris-buffer. Soret and Q bands are marked into the absorption spectrum.
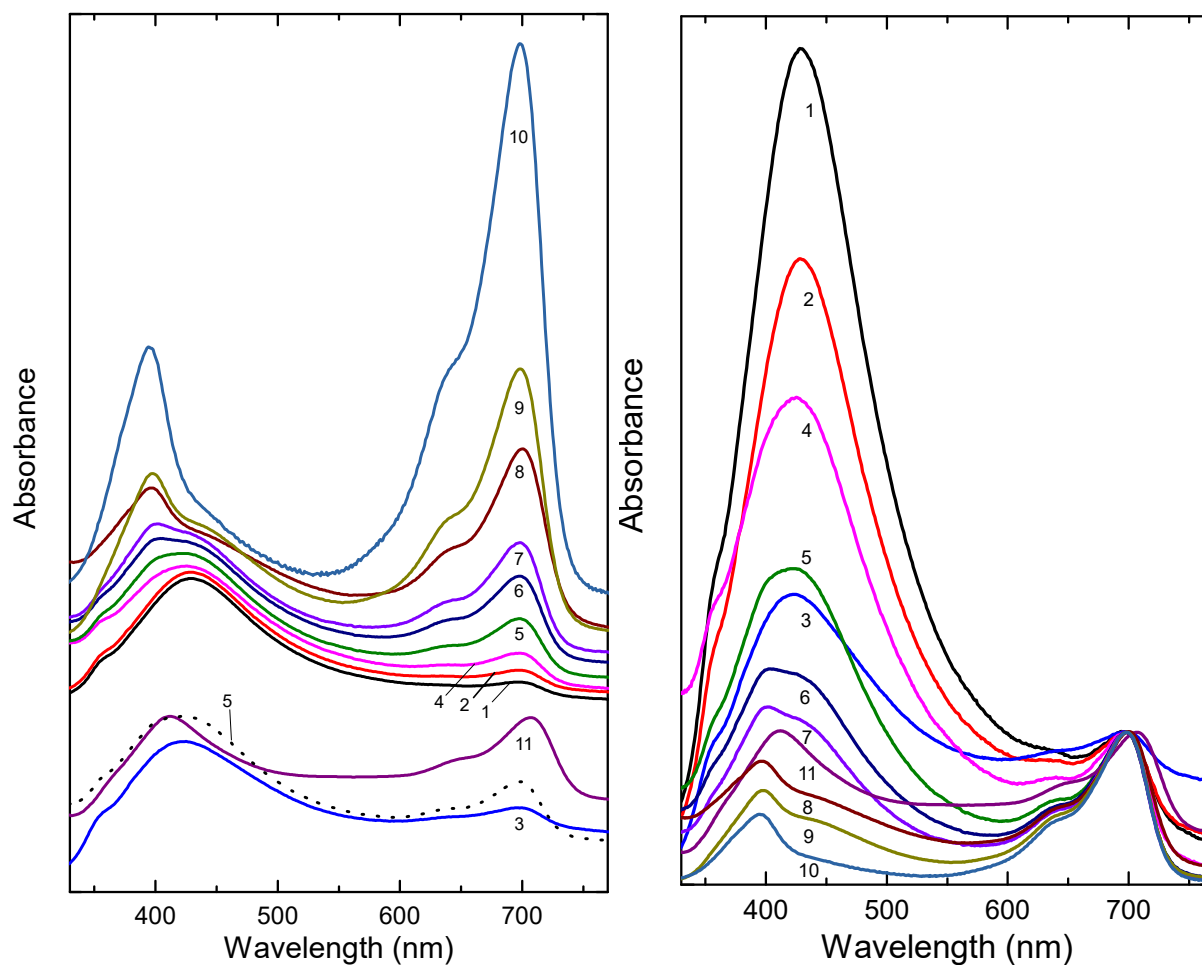
Figure 2: Total absorbance of the AgNP-CBDmon samples normalized at (left) 400 nm and (right) 700 nm. An increasing offset is added into the left spectra to visualize the differences. The sample number is located next to the absorption spectrum.
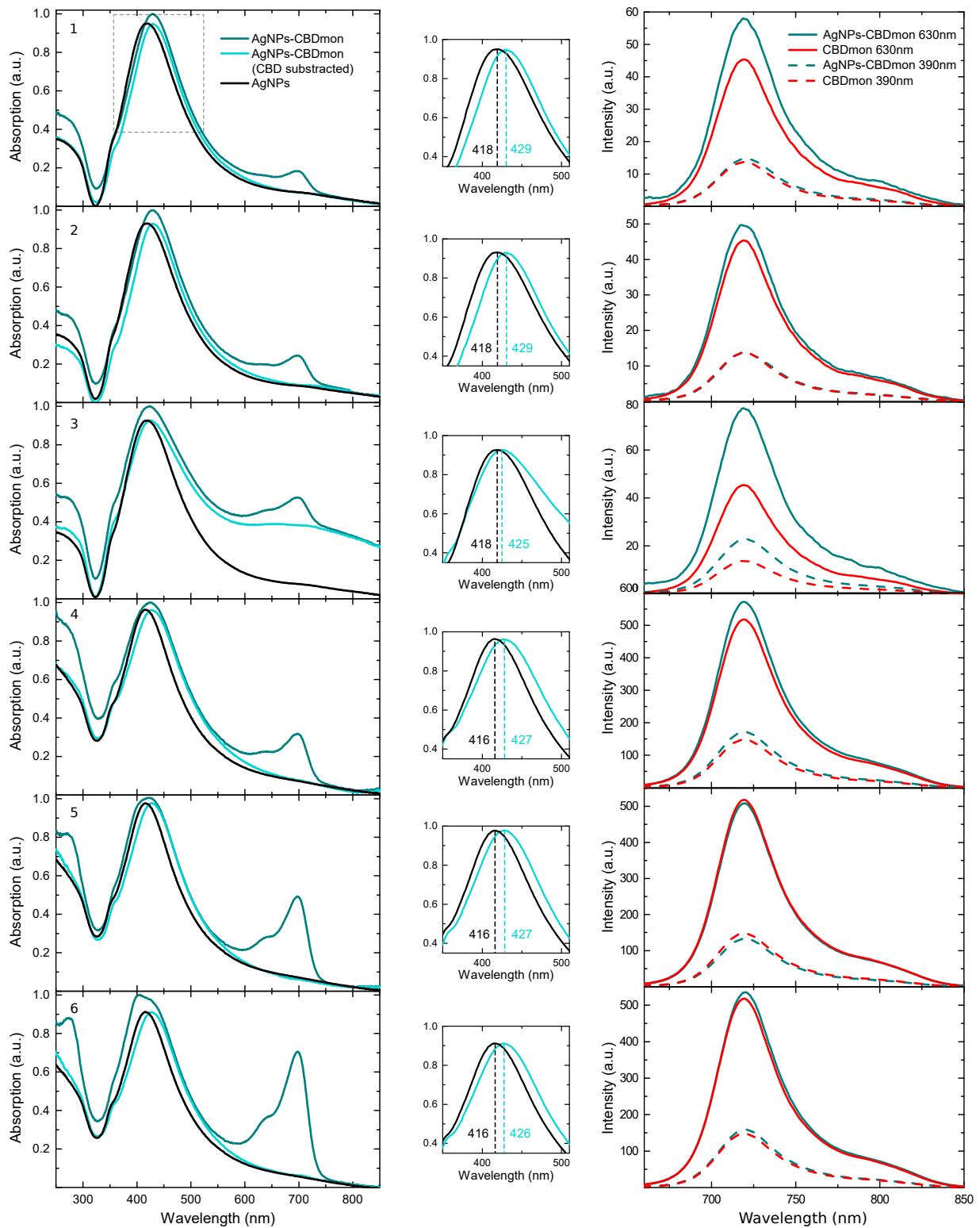
Figure 3: On the left, total absorption spectrum of the synthesized complex (cyan), total absorption with CBDmon substracted (light cyan) and absorption spectrum of AgNPs (black). On the middle, zoomed view of the LSPR maximums AgNPs. On the right, fluorescence intensities of CBDmon (red) and AgNP-CBDmon (cyan). The sample number is located on the left upper corner of a row.
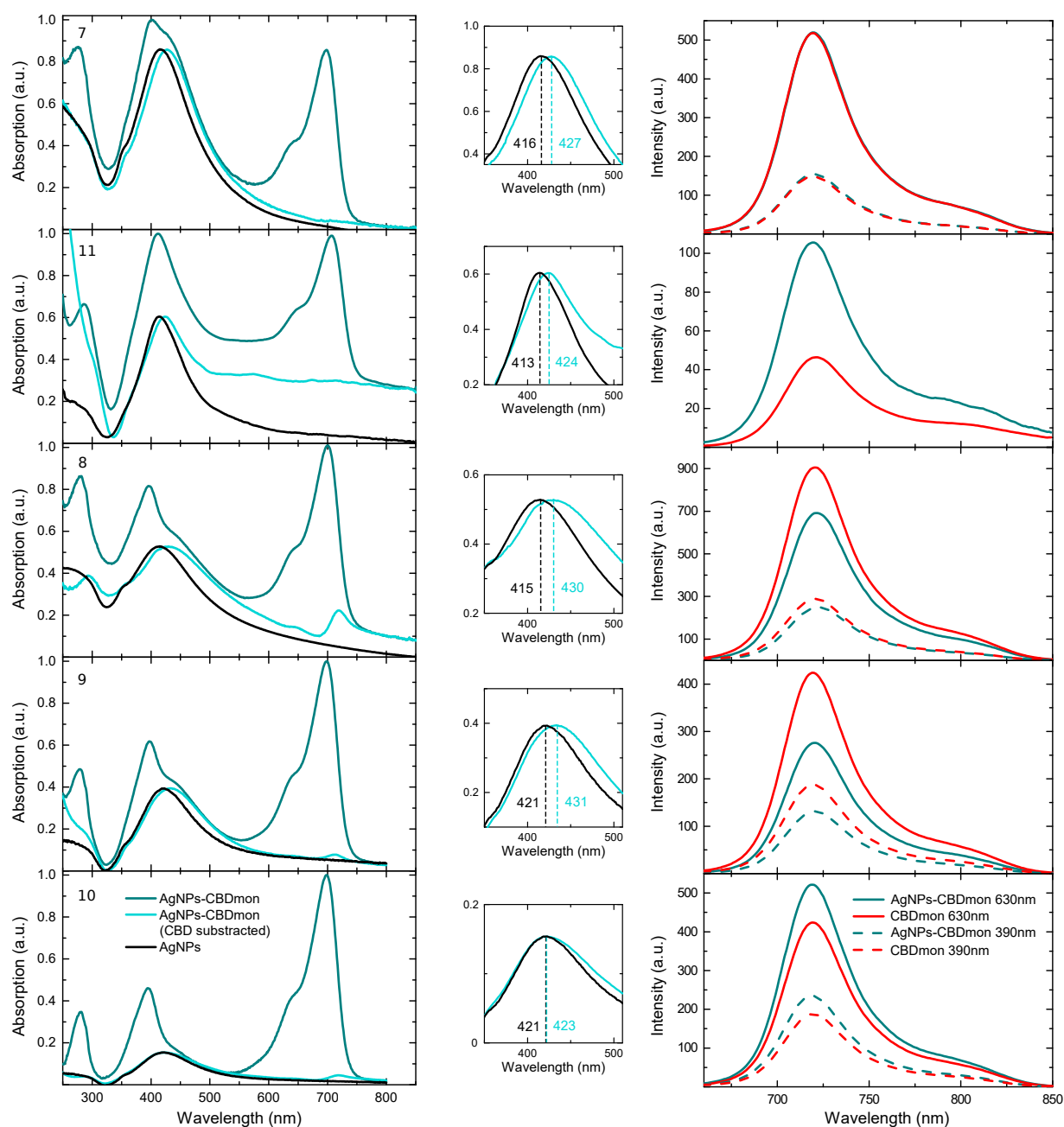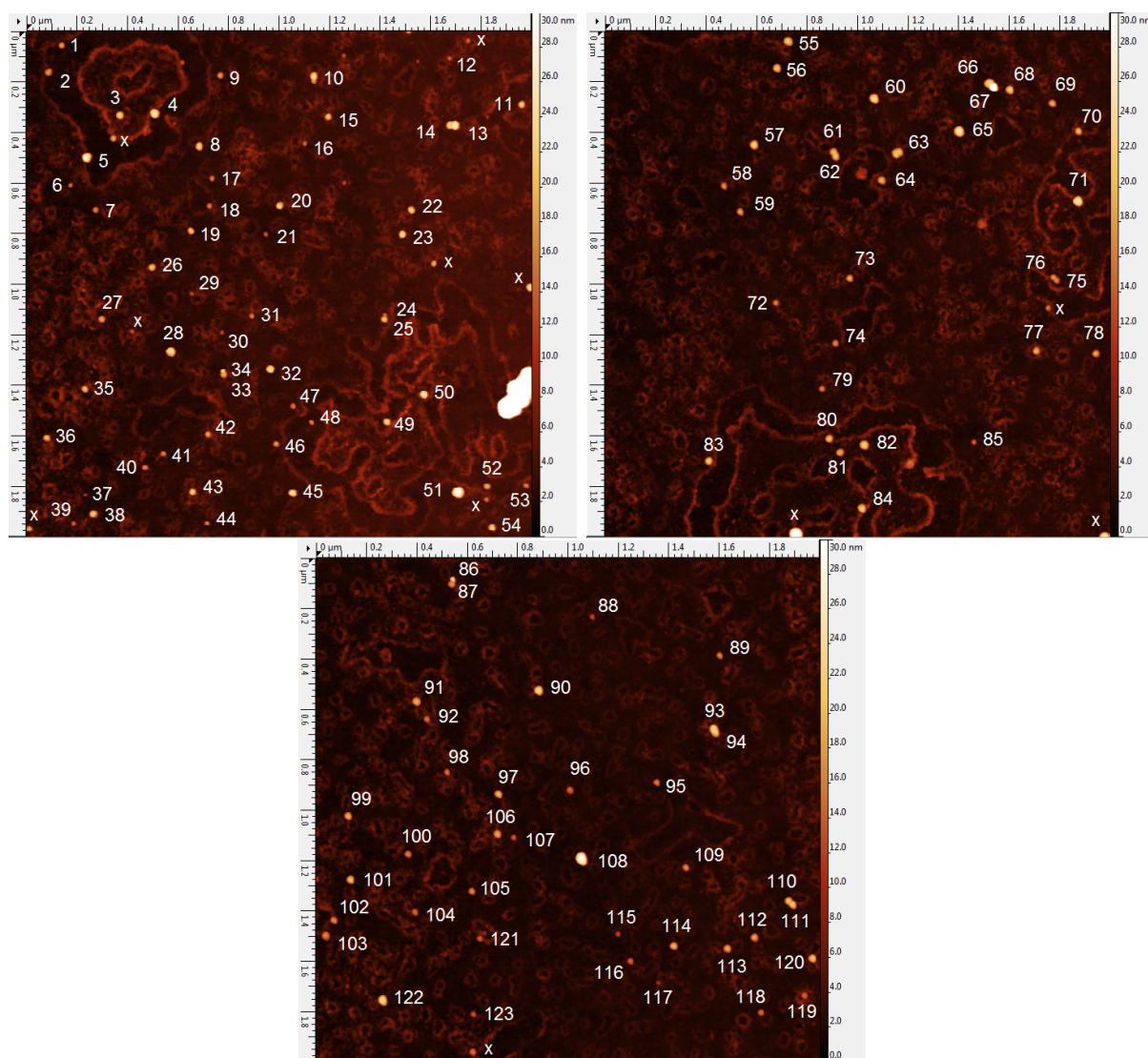
Figure 4: On the left, total absorption spectrum of the synthesized complex (cyan), total absorption with CBDmon substracted (light cyan) and absorption spectrum of AgNPs (black). On the middle, zoomed view of the LSPR maximums AgNPs. On the right, fluorescence intensities of CBDmon (red) and AgNP-CBDmon (cyan). The sample number is located on the left upper corner of a row.

Figure 5: The measured AgNPs with no BCML. Individual NPs were numbered and the height profile of the particle was characterized. The height distribution of the NPs is presented in Fig 7.
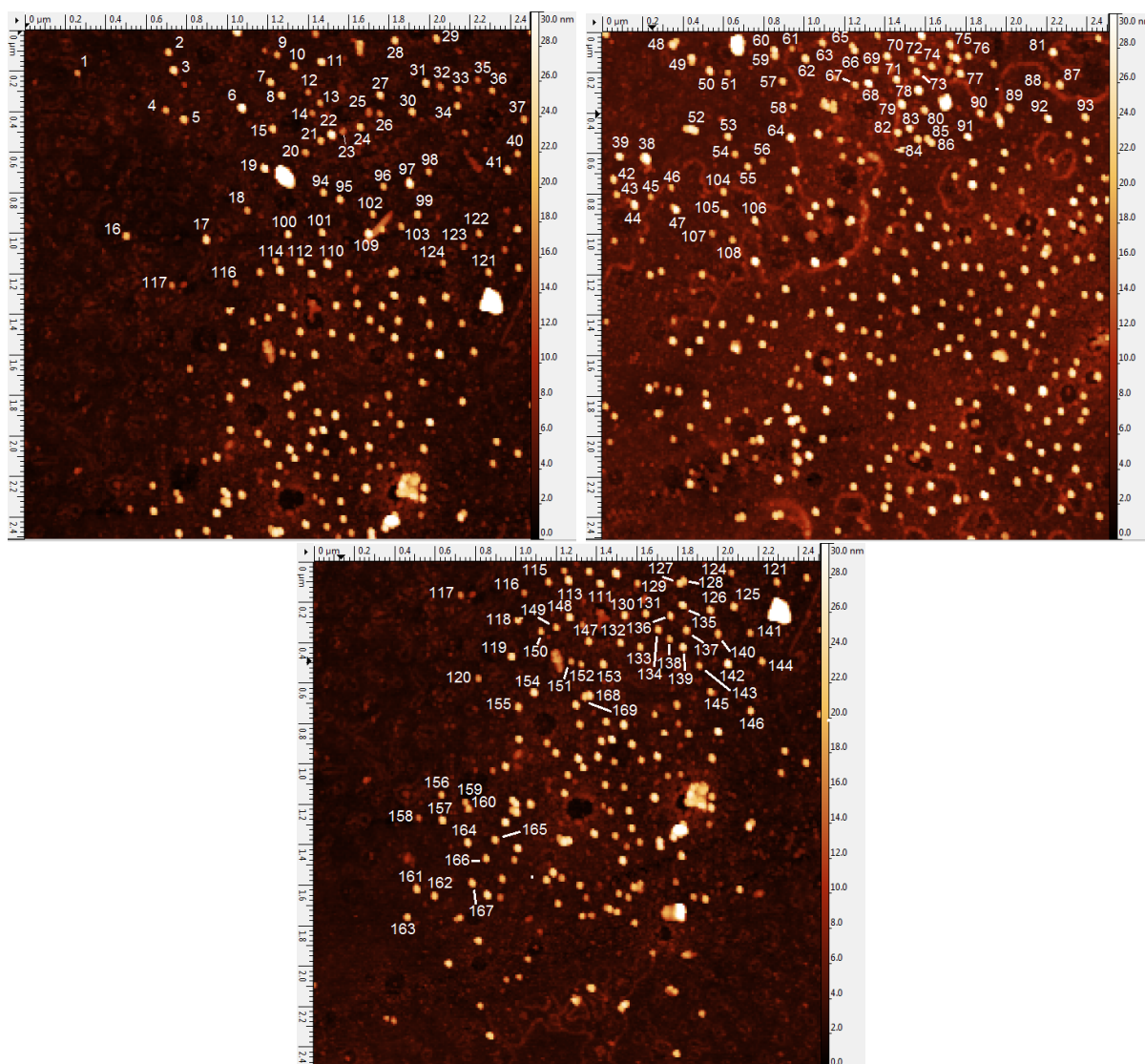
Figure 6: The measured AgNPs with BCML attached. Individual NPs were numbered and the height profile of the particle was characterized. The height distribution of the NPs is presented in Fig 7.
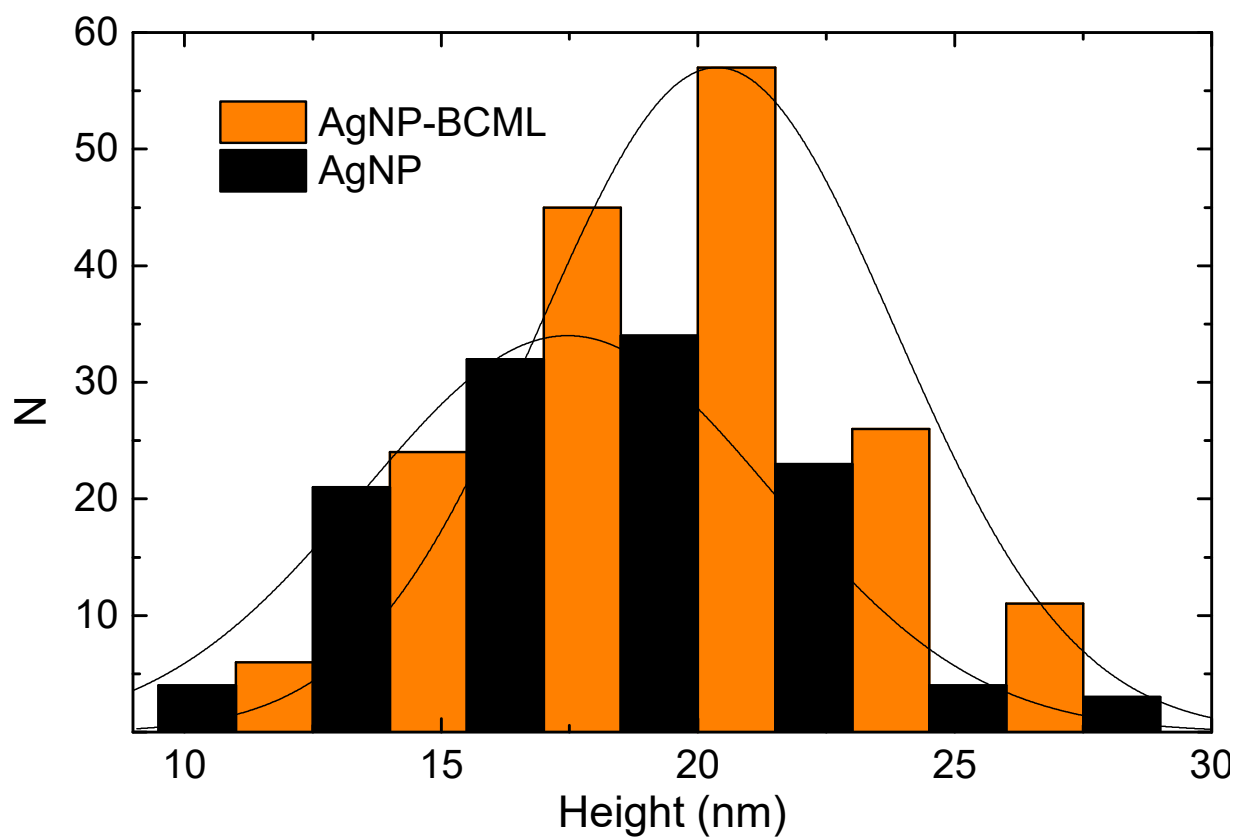
Figure 7: The height distribution of AFM measured NPs with calculated Gaussian distribution. The parameters of the fits were AgNP: $h_c = 17.461$ nm, $\sigma = 3.984$ nm and AgNP-BCML: $h_c = 20.369$ nm, $\sigma = 3.473$ nm.
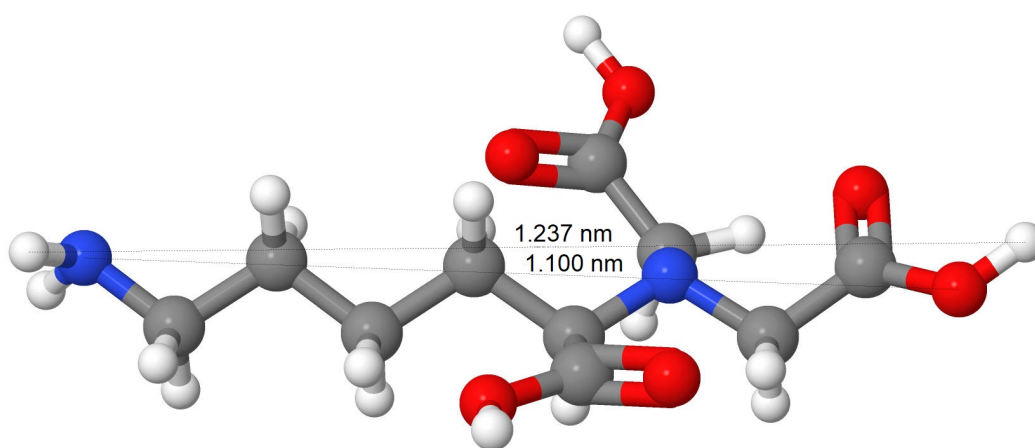

Figure 8: Optimized atomic structure of the used ligand BCML with the computationally measured lengths of the molecule (Jmol).
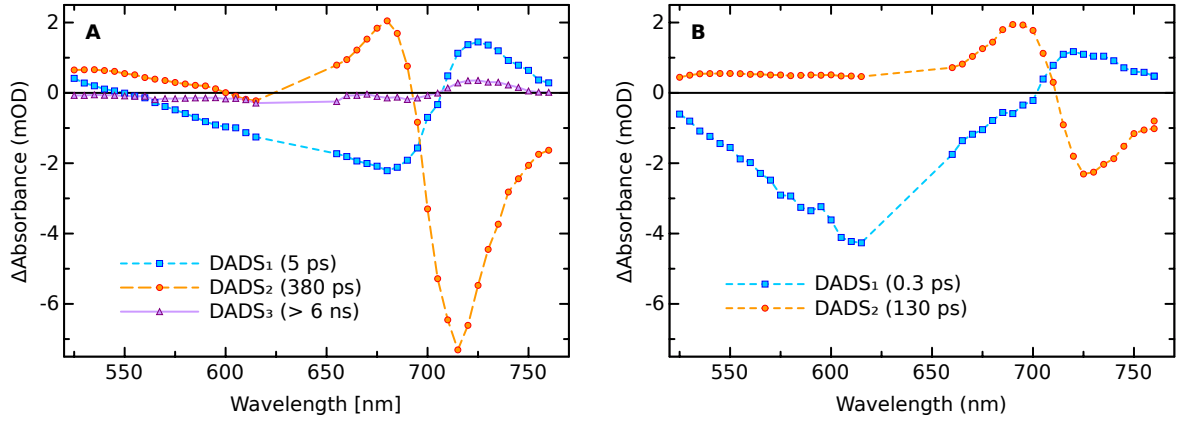
Figure 9: Decay-associated difference spectra (DADS) of (A) CBDmon and (B) AgNP-CBDmon samples.

Table 1: **Properties of the prepared samples with measured quantum yields and calculated decay fits for TCSPC and pump-probe.**[+]

#	c_{CBD} (nM)	$\dfrac{c_{CBD}}{c_{Ag}}$ $\cdot 10^4$	F_{max} (nm)	ϕ_{390} (%)	ϕ_{630} (%)	B_{390} (%)	B_{630} (%)	TCSPC τ_{375} (ps)	τ_{660} (ps)	pump-probe τ_1 (ps)	τ_2 (ps)	τ_3 (ns)
0	2390	-	719	0,76	2.9*	100	100	380&580[A]	390&620[B]	5	380	> 6
1	550	11.4	719	0.84	3.8	365	174	-	-			
2	660	15.5	719	0.78	3.2	374	125	-	-			
3	380	8.6	719	1.3	5.2	649	200	-	-			
4	810	20.9	719	0.88	3.2	589	149	-	-			
5	1790	40.3	720	0.69	2.8	460	132	-	-			
6	2150	70.5	720	0.82	3.0	546	140	-	-			
7	1800	77.7	720	0.80	2.9	530	135	-	-			
8	1490	105	721	0.66	2,2	338	78	-	316			
9	2620	238	721	0.53	1.9	296	73	-	-			
10	1130	406	720	0.94	3.6	516	129	330	346			
11	820	85.3	720	-	6.3	-	5017	-	-	0.3	130	-

[+] c_{CBD} and c_{Ag} are concentrations of CBDmon and AgNPs in the prepared sample, F_{max} is the fluorescence maximum and ϕ is measured quantum yield at 390 nm or 630 nm. B_{390} and B_{630} are determined brightnesses in respect to the free CBDmon brightness. τ_{375} and τ_{660} are single exponential lifetimes for TCSPC and τ_1, τ_2 and τ_3 lifetimes for pump-probe. [A,B] Percentual contributions to the lifetime are 72% and 28% for [A] or 67% and 33% for [B]. (Bhattacharya et al., 2014)
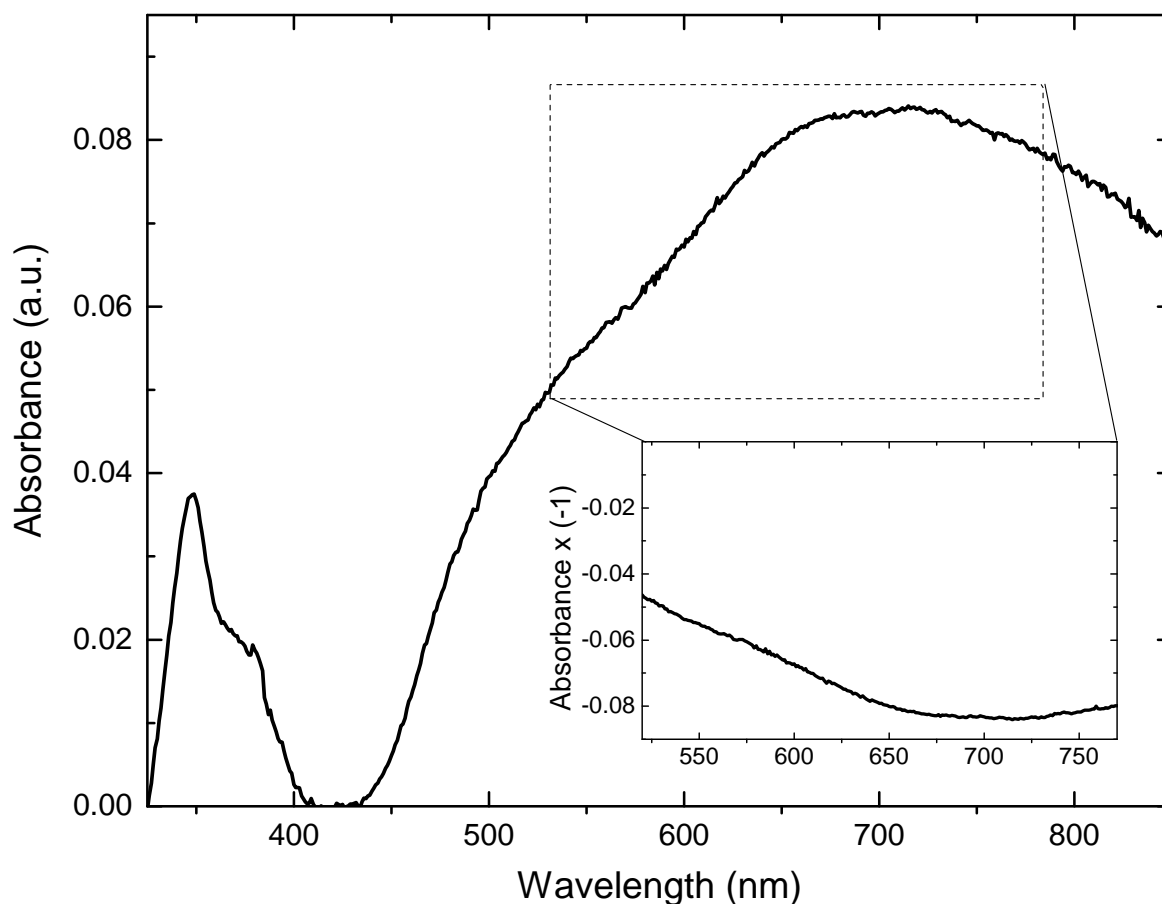
Figure 10: (Big) Absorption spectrum of aggregated AgNPs in AgNP-CBDmon sample 3. The spectrum is calculated by substracting the maximum absorption of AgNPs and CBDmon from the total sample absorption. The maximum of AgNPs is adapted manually from the original AgNP absorption spectrum. (Small) The complement of the resulting spectrum on the area of 520 nm-770 nm which is the same as in time-resolved absorption measurements.
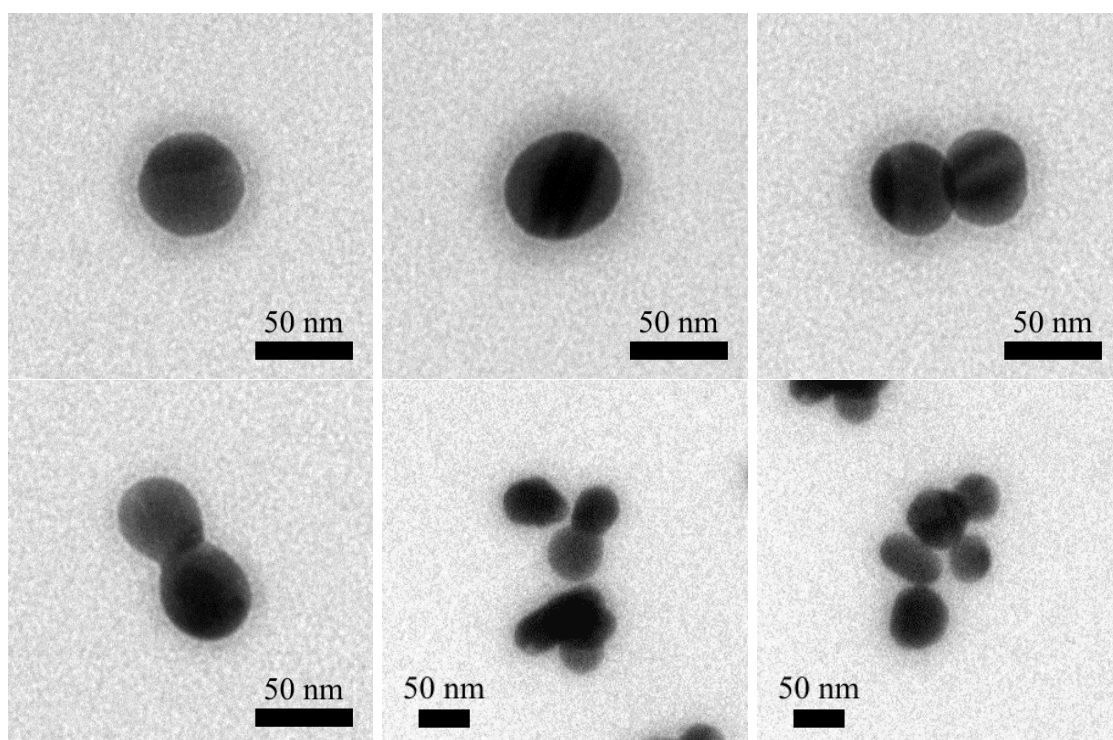
Figure 11: TEM images of AgNPs which have potentially bound CBDmon on the surface. CBDmon forms a thin blurred veil around the NPs with a diameter of approximately 8 nm.